Master RADMEP

Master Radiation and its Effects on Microelectronics and PhotonicsTechnologies (RADMEP)

Investigate the radiation response of Heterojunction Bipolar Transistors: impact of X-ray irradiation on DC and Low Frequency Noise characteristics

Master Thesis Report

Presented by

Adebabay Belie Ayenew

and defended at

University of Jean Monnet

12/09/2023

Academic Supervisor: Prof. Frédéric Saigné

Host supervisors: Prof. Fabien Pascal

Prof. Bruno Sagnes

Jury Committee: Prof. Arto Javanainen, University of Jyvaskyla (JYU)

Prof. Dr. ir. Paul Leroux, Ku Leuven

Prof. Frédéric Saigné, University of Montpellier (UM)

Prof. Sylvain Girard, University of Jean Monnet (UJM)

Investigate the radiation response of heterojunction bipolar transistors: impact of X-ray irradiation on DC and low frequency noise characteristics.

by

Adebabay Belie Ayenew

This thesis is submitted as a partial fulfillment of the requirement for master's degree in Radiation and its Effects on Microelectronics and PhotonicsTechnologies (RADMEP)

August, 2023

Declaration

I have completed my master thesis at Institute of Electronic and systems (IES), University of Montpellier on the title “Investigate the radiation response of heterojunction bipolar transistors: impact of X-ray irradiation on DC and low frequency noise characteristics. And I hereby certify that this is my original work executed solely by myself and has not previously been submitted to any institution to get any other degree or certificate. Any guidance or help I received throughout my studies has been duly acknowledged.

Acknowledgment

First and foremost, I would like to express gratitude to God, the Almighty, for his wisdom, perseverance, and strength.

I would like to express my deepest gratitude to my supervisors, Prof. Fabien Pascal, Prof. Bruno Sagnes, and Prof. Frédéric Saigné, for their dedicated advice, close help, and warmest treatments, besides the ideas and suggestions they have been sharing with me. I would like to thank Prof. Jérome Boch, Prof. Alain Hoffmann, and Mr. Tadec Maraine for their enormous deeds throughout my thesis. My special thanks go to the RADIAC team at IES, University of Montpellier, as the X-ray facility was always available when I needed it.

I would like to thank all my professors. This achievement would have remained unattainable without their dedication and generosity.

My utmost gratitude is extended to all RADMEP academic coordinators and international coordinators for giving me this opportunity and supporting me throughout my study. I am grateful to the European Commission for financing my whole master's study.

Although no words can express my gratitude, I am deeply thankful to my family for their patience and unreservedly continuous encouragement during my study.

Abstract

SiGe HBTs have emerged to meet the burgeoning demand of wireless communication and high-speed niche applications at a compelling cost advantage. The high integration capability of SiGe technology with CMOS provides a favorable opportunity to leverage the advantages of both technologies. But in recent years, the fast scaling of transistor dimensions has increased the 1/f noise and sets a minimum signal level of electronic devices. In addition, the detrimental effects of radiation on the performance and reliability of electronic devices have been an issue in the radiation society. Consequently, this is my main motivation to characterize, model and analyze the SiGe:C HBT devices to design rad-hard devices and to find a solution that reduces low-frequency noise.

I have evaluated the impacts of x-ray irradiation on the DC characteristics and low-frequency noise of 55 nm advanced SiGe:C HBTs. The HBTs, which exhibit a f_T/f_{Max} of 320/370 GHz, are issued by STMicroelectronics. Three samples, which covers an emitter area range of 0.2× 5 μm² to 0.42 × 10 μm² were irradiated to 240 krad(air), 280 krad(air) and 520 krad(air), which is far more than the prior study on this device (i.e., 151 krad (air)). The DC parameters such as forward Gummel characteristics, current gain (hFE), relative excess base current (Δib/ib) and relative excess collector current (Δic/ic) were examined before and after irradiation. Moreover, the impacts of annealing at 100 ℃ and 130 ℃ have been evaluated to examine the possible recovery mechanisms of induced radiation traps.

Concerning low frequency noise (LFN) the dependence of base current noise spectral density (Sib) of 1/f noise and generation-recombination noise (g-r noise) on base current is evaluated. To extract Kb, a figure of merit representing the 1/f noise amplitude, and locate the low-frequency noise sources, the impact of emitter geometry and collector doping is analyzed using compact SPICE modeling.

I present that the radiation- induced traps majorly affect the low injection region of the base current. This is confirmed by the plot of Δib/ib with TID at different base emitter voltages, Vbe, and our post-irradiation model. In addition, the dependence of Δib/ib with emitter geometry locates the induced-radiation trap centers. The compact SPICE modeling of the 1/f noise of the device under test (DUT) shows that Sib is proportional to the quadratic dependence of base current and Kb is in the range of 10^{-9} μm².

Keywords: Annealing, Gummel plot, low frequency noise (LFN), SiGe: C HBT, total ionizing dose (TID), X-ray irradiation

Table of contents

List of Figures

List of tables

List of Abbreviations

Ae	emitter area
BiCMOS	bipolar complementary metal oxide semiconductor
BJT	bipolar Junction transistor
DTI	deep trench isolation
g-r	generation- recombination
HBT	heterojunction bipolar transistor
HS	high speed
HV	high voltage
LFN	low frequency noise
MV	medium voltage
Pe	emitter perimeter
Pe/Ae	emitter perimeter-to-emitter area ratio
PSD	power spectral density
RF	radio frequency
RTS	random telegraph signal
SIC	Selectively implanted collector
STI	shallow trench isolation
TID	total ionizing dose

Chapter 1. Introduction

1.1 SiGe: C heterojunction bipolar transistor (HBT)

Since the discovery of the bipolar junction transistor in 1947 at Bell Labs, silicon has been dominating and playing a pivotal role in the semiconductor industry due to its easily grown, high degree of integration, abundance of availability, and excellent thermal properties. Nevertheless, silicon exhibits limited carrier mobility, thereby failing to satisfy the burgeoning demand of wireless communication and various high-frequency niche applications. At high electric fields, for example, the maximum velocity of carriers in silicon is approximately 1×10^7 cm/sec [1]. Consequently, promising SiGe HBTs have emerged to address these issues. It is interesting that SiGe HBTs don't require a complex manufacturing process or equipment compared to III-V devices [2], which exhibit high saturation velocity and carrier mobility. Moreover, the high integration capability of SiGe HBTs with CMOS technology provides a favorable opportunity to leverage the advantages of both technologies, thereby providing a compelling cost advantage. This attracts European IC companies such as IHP, NXP, Infineon, and STMicroelectronics to keep contributing to the emergence of Si-based THz.

1.2 SiGe HBT characteristics

SiGe HBTs are a bread of bipolar transistor that utilizes the concept of band gap engineering by incorporating germanium in the base of the transistor. Band gap engineering was introduced by Kroemer in the 1950s [3] and pioneered in 1987 [4]. As depicted in Fig. 1, the efficiency of electron injection greatly increases because of the Si and Ge energy band offsets at the Emitter-Base junction. Consequently, this leads to significant increases in collector current and an inherently higher current gain compared to Si-based BJT [5]. Moreover, equation (1) presents the current gain of SiGe HBT and Si BJT as:

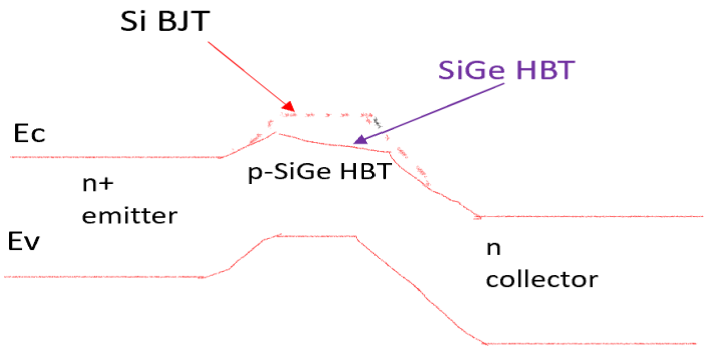

Fig. 1 Energy band diagram of SiGe:C HBT and Si BJT

$$\frac{\beta_{SiGe,unif}}{\beta_{Si}} \approx e^{\Delta E_{EB}/kT} \quad (1)$$

where β_{SiGe}, unif and β_{Si} are the current gain of uniformly graded SiGe HBTs and Si BJTs respectively, ΔE_{EB} is the bandgap difference between emitter and base for a uniformly

graded doping [6], k = 1.38×10^{-23} J/K is the Boltzmann constant and T is the absolute temperature

In most circuit application areas, the inherent high current gain of SiGe HBTs is more than adequate; this creates room for IC industries to play with the tradeoff between base doping and current gain. In fact, increasing base doping lessens the base transit time, and improves the crucial high-frequency application parameters, namely the cutoff frequency, fc, and maximum oscillation frequency, fmax, [5]. Furthermore, this also enables SiGe HBTs to exhibit better noise performance than Si BJT. Fig. 2 compares the collector current and cutoff frequency of the two technologies.

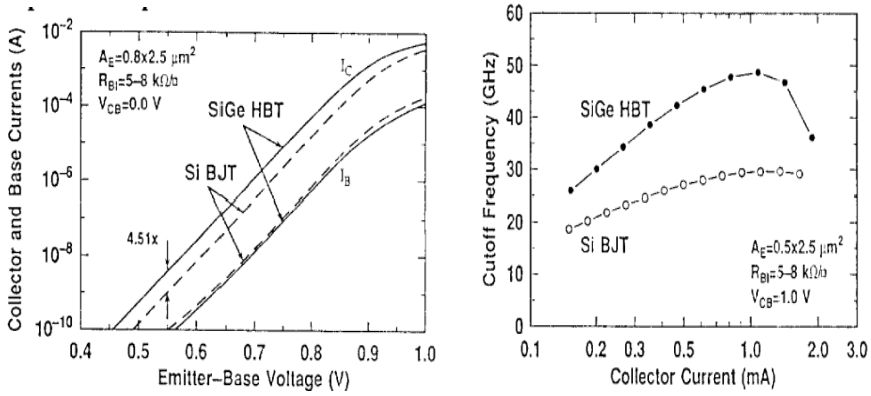

Fig. 2 I-V characteristics(left) and cutoff frequency(right) of SiGe HBT and Si BJT. Adapted from [5].

1.3 LFN components in bipolar transistors

Although extensive studies have been done on the LFN of electronic devices, it is still a hot topic that needs further investigation. The primary reasons for studying LFN are as follows: Firstly, LFN serves as a useful tool for identifying defects and assessing the reliability of materials [7]. Secondly, LFN will be upconverted to high frequency due to the nonlinear nature of electronics devices, which can affect the performance of RF mixers, oscillators, and power amplifiers. The fast scaling of transistor dimensions has increased the 1/f noise and sets a minimum signal level of electronic devices.

In this section, types of noise, physical and compact modeling of LFN will be presented. Noise is considered undesirable as it fluctuates the current or voltage of an electronic device, which stems from the random fluctuation of charge carriers. Generally, there are two types of noise: white noise and excess noise. Unlike the latter, the former is not frequency dependent and represents the minimum noise of the device. It is further divided into two divisions: thermal noise and shot noise. Excess noise is classified into three categories: generation-recombination (g-r) noise, 1/f noise, and Random Telegraph signal (RTS) noise.

Thermal noise originates from the random motion of charge carriers. The current, Si, or voltage, Sv, power spectral density of thermal noise is expressed as:

$$Si = \frac{4kT}{R} \tag{2}$$

$$Sv = 4kTR \tag{3}$$

where R is the access resistance of the conductor [8].

Shot noise: the manifestation of shot noise arises due to perturbations related to direct current flow because of the presence of charged particles traversing the potential barrier. The power spectral density of shot noise at low frequencies is expressed as:

$$Si = 2qI \tag{4}$$

Remarkably, SiGe HBTs have an inherently larger current gain than Si BJTs. This explains why SiGe HBTs have a smaller base current shot noise than Si BJTs for the same collector current. Additionally, SiGe HBTs exhibit smaller base current shot noise than Si BJTs at the same current gain [9].

The second type of noise source is excess noise, which is generated due to structural or individual defects, such as impurities located at the interface of semiconductor oxides. This sort of noise is associated with fluctuations in the conductivity of the material, and it has the general characteristic of increasing spectral density at low frequencies. By improving the quality of the material, it is feasible to reduce defects and impurities in the material, which reduces excess noise. Unlike white noise, excess noise is frequency dependent. It is classified into three basic categories based on their characteristics [10]: generation-recombination (g-r) noise, random telegraph signal (RTS) noise, and flicker noise (1/f noise).

G-r noise stems from free carrier number fluctuations between states in different energy bands. The free carrier number fluctuation originated because of the trapping and detrapping processes of the carriers [11]. The power spectral density, PSD, of g-r noise is expressed as:

$$\frac{S_N(f)}{N^2} = 4\frac{\overline{\delta N^2}}{N}\frac{\tau}{(1+2\pi f\tau)^2} \tag{5}$$

where N is the average number of free carriers, τ is the lifetime of a free carrier, $\overline{\delta N^2}$ is the variance of carrier number fluctuation, and f is frequency. The Lorentzian spectrum can be depicted in a seamless manner with a constant plateau at low frequencies and rolldown as f^2 until the cutoff frequency.

Random-telegraph-signal (RTS) noise originates from the trapping and de-trapping of charge carriers at the active trap level. According to some scholars, this even happens with a few charge carrier fluctuations in contrast to g-r noise and triggers the current to switch between two or more states.

Flicker noise, also known as 1/f noise, has a PSD proportional to $f^{-\gamma}$ where γ varies from device to device in the range 1 ± 0.1 [12]. Flicker noise is believed to be generated from the fluctuation of a material's conductivity, which is expressed as:

$$\sigma = q\mu n \tag{6}$$

Even though many research has been done on 1/f noise, the physical origin of flicker noise still be a topic of controversy. It is widely held that it stems from charge carrier

fluctuation and their mobility. The latter stems from lattice scattering [12], and the former is associated with structure-state theory [13].

1.4 Physical models of Excess noise Sources

1.4.1 1/f noise physical models

The origin of 1/f noise is a subject of research interest that needs more investigation. Numerous scholars have proposed various models to quantify the low-frequency noise of devices. Generally, those models are classified into two categories based on the relation of 1/f noise with bias current, Ib. The first model is associated with the quadratic dependence of 1/f noise on Ib, which is notably prevalent in modern SiGe HBTs. On the other side, the second model is related to the linear dependence of 1/f noise on Ib and is associated with structure-state theory. As I am addressing the 1/f noise model in SiGe HBTs, I shall focus on the former model by leaving the latter model to the reader.

The Ib^2 models of 1/f noise comprise 1) superposition of g-r noise, 2) a two-step tunneling model, 3) a tunneling fluctuation model, 4) a tunneling assisted trap model, 5) surface noise due to carrier density fluctuations, and 6) a random walk model. The summary and some parameter dependencies of these models are presented in Table 1.

Model	N_T	t_{ox}	T	Geometry	equation	References
1	N_T	-	complex	A_e^{-1}	$\frac{Sib}{Ib^2}=\frac{K_{fN_{T,dec}}}{A_e f}$	[15],[16]
2	N_T	t_{ox}^2	T^{-1}	$A*_e^{-1}$	$\frac{Sib}{Ib^2}=\frac{q^4}{\ln[\frac{\tau(xo)}{\tau(0)}]2k\varepsilon_{ox}^2}\frac{N_T t_{ox}^2}{TA_e^* f}$	[17],[18]
3	-	t_{ox}^3	complex	A_e^{-1}	$\frac{Sib}{Ib^2}=\frac{1}{[1+\sqrt{\frac{kT}{2\pi m_p}}T_{p,ox}(\frac{1}{\zeta_m}+\frac{W_m}{D_m}+\frac{W_p}{D_p})]^2}\frac{4\pi q m_p \tan\delta}{3h^2}\frac{t_{ox}^3 T}{f\varepsilon_{ox}V_O A_e}$	[19]
4	N_T	-	T^{-1}	$(PW_{sc})^{-1}$	$\frac{Sib}{Ib^2}=\frac{q^4\lambda}{kC_{sc}}\frac{N_T^*}{T(PW_{sc})f}$	[20]
5	N_T	-	T	A_s^{-1}	$\frac{Sib}{Ib^2}=\frac{kTN_T}{\theta A_s f}$	[21]
6	N_T^{-1}	-	-	A_e^{-1}	$\frac{Sib}{(I_{so}\frac{I_b^{2m/n}}{I_{bo}^{2m/n}})^2}=\frac{0.1}{A_e f N_{IT}}$	[22], [23]

Table 1 Ib^2 physical models of 1/f noise

1.4.2 G-r physical models

This type of noise is presently being witnessed in modern transistors. The current spectral density is modeled by:

$$Si=\frac{I^2}{n^2V}4n_t f_t(1-f_t)\frac{\tau}{1+w^2\tau^2} \tag{7}$$

where V and I are the volume of semiconductor and the mean value of the current bias, respectively; f_t is the probability of the trap level to be occupied; n is the charge density of carriers; and τ is the trapping/detrapping time constant [14], which is expressed as:

$$\tau=\frac{T_a}{\sigma_n v_{th}(T_r)N_c(T_r)T^2}\exp(\frac{E_c-E_t}{kT}) \tag{8}$$

where $E_c - E_t$ is the energy level of a trap, $\sigma_n$is the effective cross section of an electron at room temperature, and v_{th} is the electron thermal speed [14].

The current spectral density of the g-r noise, Si is directly related to I^2 and inversely proportional to the volume, V. The Lorentzian spectrum exhibits a constant plateau until the cutoff frequency, fci, at which the plateau is reduced by half. The cutoff frequency is expressed as:

$$f_{ci} = \frac{1}{2\pi\tau} \tag{9}$$

1.5 Compact models of 1/f and g-r noise

Investigating and evaluating the noise levels of bipolar transistors through physical models of low-frequency noise is not trivial. It needs to understand each type of model. Therefore, it is necessary to employ compact models of excess noise by using SPICE modeling, which helps circuit designers investigate the effects of excess noise in their designs. In addition, SPICE modeling of excess noise can be used to compare the noise levels of different technological devices. For this study, we only present the two SPICE models of LFN: 1/f noise SPICE modeling and g-r noise SPICE modeling.

1.5.1 1/f noise SPICE model

In bipolar and heterojunction transistors, it has been examined that the base and collector currents may exhibit 1/f noise. However, it is noteworthy that the PSD of 1/f noise due to base current dominates, as elaborated in Section 1.3 for shot noise. Consequently, hereafter only the 1/f noise caused by base current will be discussed. A typical base current spectral density measured on HBTs during this thesis is given in Fig. 3. Note that the cut-off frequency above 10 kHz is due to the low-noise amplifier characteristics.

The base current spectral density, S_{ib}, of 1/f noise is presented in three SPICE parameters, Kf, Af and γ, as:

$$S_{ib(f)} = Kf\frac{{I_B}^{Af}}{f^{\gamma}} \tag{10}$$

where Kf is given by Sib at 1Hz divided Ib^{Af}, I_b is an input base current, Af is the evolution of base current with respect to S_{ib} at a given frequency, and γ is the evolution of frequency. The steps to extract the SPICE parameters are:

Step 1: After plotting the spectrum with frequency, check the slope to see if it is close to -1. For example, γ is equal to 1 for the spectrum shown in Fig. 3.

Step 2: To extract Af , S_{ib} at 1Hz is plotted for different inputs, I_b. When Af = 2, it is believed to be due to carrier number fluctuation [7], [24], and carrier mobility fluctuation when Af = 1 [25]. For SiGe HBTs, Af is close to 2 [25], [26].

Step 3: After γ & Af parameters are extracted, Kf will be determined by the expression:

$$K_f = \frac{S_{ib} \text{ at } 1Hz}{{I_b}^2} \tag{11}$$

Usually, K_f is proportional to 1/Ae which Ae is emitter area. And if it is that so, it is interesting to investigate K_b, which is the product of K_f and A_e [27], [28]. The figure of

merit, K_b, helps to compare the 1/f noise performance of various technology node electronic devices.

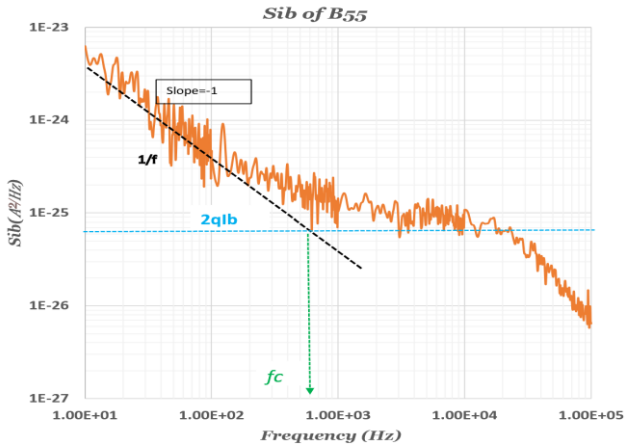

Fig. 3 Example of gamma (γ) extraction.

1.5.2 G-r SPICE model

The SPICE model of g-r noise can be represented by the superposition of g-r noises as follows:

$$S_{ib} = \sum_{i=1}^{n} \frac{A_{i,}(I_b)}{1+\left(\frac{f}{f_{c,i}(I_b)}\right)^2} \quad (12)$$

where $f_{c,i}$ and A_i (Ib) is the cutoff frequency and magnitude or plateau of individual g-r components, respectively [29]. Fig. 4. presents a g-r noise with a plateau close to 10^{-22} A^2/Hz and fc near to 70 Hz at Ib =50 nA.

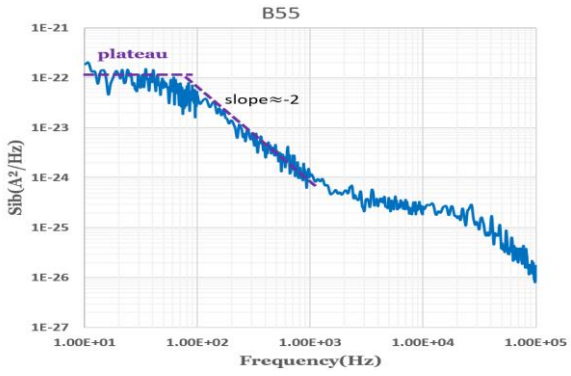

Fig. 4 Example of spectrum with a g-r noise component (Lorentzian shape)

1.5 Radiation effects on electronics devices

The detrimental effects of radiation on electronic devices have been a major issue in the radiation society, as it has a negative impact on the performance and reliability of electronic devices. Generally, the radiation environment can cause two effects on microelectronic devices, namely the single event effect (SEE) and the dose effect (DE).

The former happens when a single particle ionizes a semiconductor device and causes either permanent or temporary damage, whereas unlike the former, the latter happens when particles ionize a semiconductor device and cause either displacement damage or total ionizing dose (TID). For this thesis, I will only focus on the effects of TID.

When particles or photons strike the oxide of a semiconductor device, electron-hole pairs are created. The generated electron-hole pairs begin to recombine, and the uncombined electron will move away from the oxide due to its high mobility. The holes will jump through hopping and later will create oxide and interface traps [1], [30]. The traps lead to an increase in low frequency noise and degradation of current gain in bipolar transistors, and in the case of MOS, it is a cause for an increase in leakage current and shifts in threshold voltage.

1.6 Significance of this thesis

Upon completion, this thesis will help to investigate and examine the effects of x-ray irradiation on the DC characteristics and low-frequency noise of advanced SiGe: C HBTs. The thesis will make a significant contribution to the hot research topics of radiation and LFN; in addition, it gives adequate guidelines for IC designers.

1.7 Organization of this thesis

The thesis is divided into four chapters. The fundamental concepts of SiGe HBTs, LFN, and irradiation are presented in the first chapter. In addition, the first chapter also describes the scope and significance of our thesis as well as recent studies related to the effects of x-ray radiation and the LFN of SiGe: C HBTs.

The second chapter presents the methodologies that were used for my study. The device under test (DUT), experimental procedures for LFN measurements, and DC characteristics are highlighted, along with radiation and annealing methodologies.

The third chapter discusses DC characteristics and LFN of SiGe:C HBTs before and after x-ray radiation. The weekly and annealing measurement results are also presented in this chapter. The fourth chapter presents the conclusion and future work of this thesis.

1.8 State of the art

1.8.1 State of the art of LFN on SiGe HBTs

The research on LFN in SiGe HBTs has attracted the attention of many researchers for a long time, as LFN affects the performance of analog, RF mixers, and oscillator circuits.

Low-frequency noise of Si/SiGe HBTs, with ft/fmax of 60/30 GHz, was experimented on by R. Plana et al. [31] in May 1995, and their findings showed that SiGe HBTs exhibit a better low-noise performance than Si BJT. Based on their work, the cause of the noise current was trapping effects at the heterointerface between emitter and base.

For the first time, the low-frequency noise in UHV/CVD Si/SiGe HBTs was investigated in 1995. Their work revealed that, S_{ib}, has characteristics of $I_b^{1.9}$ and 1/Ae with a Kb of 2×10^{-9} μm² [32], [33] and the 1/f noises were believed to be uniformly distributed in the emitter area. The incorporation of Ge in the base didn't impact the intrinsic noise-

level, as explained by [34]. In ref [35], J. Raoult et al. have obtained a Kb value as low as 4×10^{-10} μm^2 after studying the effect of carbon on 1/f noise on 130 nm BiCMOS HBTs. In ref [36], the same group has extracted a Kb value of 7×10^{-11} μm^2 for a 130 nm BiCMOS technology.

More recently, C.Mukherjee and colleagues investigated 130nm BiCMOS HBTs in which Sib was related to Ib^2 and 1/Ae results, K_B is close to 2×10^{-11} μm^2, which is less than other SiGe HBTs and III-IV HBTs. In addition, they examined g-r noise in smaller area transistors [29] after it was confirmed by their RTS noise analysis. The work of M. Seif and colleagues compares the LFN of BiCMOS9MW (130 nm BiCMOS technology), B5T (55 nm BiCMOS technology), and B55 (55 nm BiCMOS technology). BiCMOS9MW exhibits superior low-frequency noise performance compared to the other two newer technologies, while B55 is more susceptible to g-r noise compared to the other advancements [37].

Many publications have shown that when Sib is proportional to Ib^2 and 1/Ae in bipolar transistors, the possible physical location of the 1/f noise source is the emitter area. And this was proved by the work of Bruno Sagnes and colleagues after a comparative measurement was done on the three flavors of B55, which potentially differ by their selective implanted collector doping (SIC). Remarkably, the work shows that Sib is independent of the collector structure [38].

1.8.2 State of art of effects of TID on SiGe HBTs

In recent years, SiGe HBTs have been used in many application areas, including radiation-rich environments from the low temperature range (4.2k) to the higher temperature range (300°C), with superior performance compared to Si BJT [39]. This could be due to the thin emitter-base (E-B) spacer oxide of SiGe HBTs. In addition, the STI of SiGe HBTs is believed to be thinner and physically located away from the carrier transport path. Low enhanced dose sensitivity (ELDRS) has less effect on SiGe HBTs compared to Si BJT [1]. A few research groups, including Dr. John D. Cressler's group, are conducting extensive investigations on the effects of TID on SiGe HBTs.

The radiation-induced trap centers in the oxides of SiGe HBTs, as depicted in Fig. 5, have detrimental effects on the performance of devices. The radiation-induced trap centers could potentially arise in spacer oxide, pedestrian oxide, STI, and deep trench isolation (DTI). The resulting induced radiation traps are a cause for the increase in base current [1], degradation of current gain (i.e., due to a negligible increase in collector current) [40], and increase in LFN [41].

To identify the possible physical location of radiation-induced trap center sources, forward Gummel plots and inverse Gummel plots (i.e., swapping of emitter and collector from the forward Gummel plot) are used [42]. The former is implemented to examine the effects of irradiation on the E-B spacer oxide [1], [40], [41] whereas the latter helps to investigate the effects of radiation on the C-B spacer oxide [43]. According to studies, the base current and low-frequency noise of SiGe HBTs are less impacted by the induced radiation trap centers located in STI than E-B spacer oxide [42]. Hence, in many publications, only the forward Gummel plot is used to examine the radiation effects on SiGe HBTs [1], [40]-[43].

As many publications have shown, the main radiation-induced trap center sources are believed to be the E-B spacer oxide. To examine the impacts of geometry on the base and collector current, they plot the excess base and collector current, which is the post-irradiation current minus the pre-irradiation current, as a function of the emitter perimeter-to-emitter area ratio (Pe/Ae). The work shows that unlike the excess collector current, the excess base current increases with Pe/Ae [44]. Thus, based on [45], larger emitter area transistors could be a candidate for radiation-rich environments without the need of intentional hardening.

The impacts of radiation on the DC characteristics of SiGe HBTs are different based on the modes of biasing of the transistor during irradiation, which have different impacts on the formation of an electric field. As evidenced by [46], the worst degradation impacts of radiation happen when the transistor is in cutoff bias. Conversely, forward and saturation modes of biasing result in less degradation.

Like biasing, radiation temperature also has different effects on the impacts of radiation. The study by Nergui and colleagues examined the impacts of radiation temperatures at elevated temperatures (130 °C, 100 °C, and 30 °C). The result revealed that the degradation decreases with radiation temperature, and the worst-case condition happened when the device was irradiated at room temperature [47].

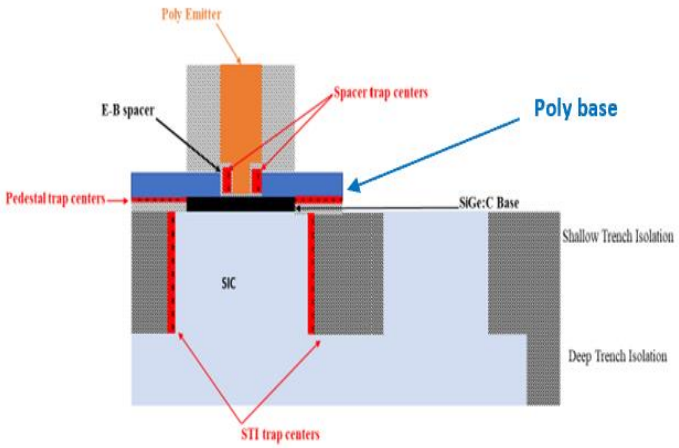

Fig. 5 Possible induced irradiation trap centers on SiGe HBT

Chapter 2. Methodology

In this chapter, the device under test will be introduced in Section 2.1, and the experimental setup of DC characteristics such as forward Gumel measurement and Ic-Vce measurements will be explained in Section 2.2. The experimental setup of LFN will be discussed in Section 2.3. Finally, the x-ray radiation methodologies, including annealing experiments, are discussed in Section 2.4.

2.1 Device under test (DUT).

The advanced SiGe:C heterojunction bipolar transistors (HBTs), a 55 nm BiCMOS (B55) with f_T/f_{Max} of 320/370 GHz [48], are issued by STMicroelectronics. B55 technology is integrated by using the polysilicon self-aligned (DPSA) technique, which is related to the selective epitaxy growth (SEG) technique of Si/SiGe: C-base epitaxy, shallow and deep-trench isolations, extrinsic base, and contact [37], [48]. Fig. 6 illustrates the transmission electron microscopy (TEM) cross section of B55 and on wafer sample. There are three flavors of B55, namely high-speed (HS), medium-voltage (MV), and high-voltage (HV), which differ by selective implanted collector (SIC) doping [48]. Moreover, the three transistors have different cutoff frequencies, maximum frequencies, and breakdown voltages, as presented in Table 2.

Parameter	NPN HS	NPN MV	NPN HV
Max f_T (GHz)	326(VCB=0.5V)	178(VCB=1V)	64(VCB=2.5V)
Max f_{Max} (GHz)	376(VCB=0.5V)	384 (VCB=1V)	269 (VCB=2.5V)
Jc(mA/μm²) at max. f_T & f_{Max}(GHz)	19	6.1	1.9
BV_{CBO}(V)	5.4	7.3	14.4
BV_{CEO}(V)	1.5	1.9	3.2

Table 2 HS, MV, and HV HBTs characteristics of 0.1×4.9 μm². Adapted from [48].

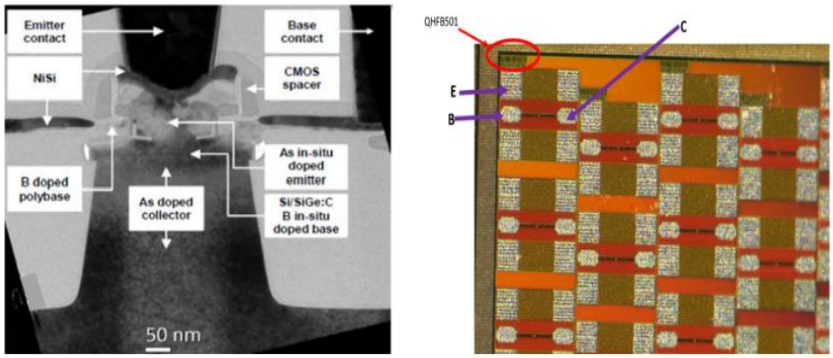

Fig. 6 TEM cross section of B55 (left) and sample (right). The left image adapted from. [27].

The single-finger CBEBC configuration of DUTs depicted in Fig. 6 has an emitter area range of 1 μm² to 4.2 μm². The geometry specifications of the DUTs are presented in Table 3.

Transistor	Name of HBT	Configuration	W_E(μm)	L_E(μm)	Area(μm²)
B55 (HS,MV& HV)	QHFB505	1 finger	0.2	5	1.0
	QHFB506	1 finger	0.2	10	2.0
	QHFB508	1 finger	0.3	5	1.5
	QHFB510	1 finger	0.42	5	2.1
	QHFB512	1 finger	0.3	10	3.0
	QHFB513	1 finger	0.35	10	3.5
	QHFB514	1 finger	0.42	10	4.2

Table 3 Specification of our Device Under Test HBTs

2.2 DC Measurements

The Gummel plot is the most convenient way to describe current-voltage characteristics of SiGe HBTs. It is a method to plot the base and collector currents (Ib and Ic) versus base-emitter voltage (Vbe) on a semi-logarithmic scale by maintaining collector-base voltage (Vcb) constant. Furthermore, this method enables us to determine the current gain and the leakage current directly in the plot.

The Ic-Vce plot is a method of plotting Ic versus collector-emitter volatge (Vce) at various base currents. This plot is implemented to distinguish the modes of operation and determine the breakdown voltage of the transistor. In this work, forward Gummel plot and Ic-Vce plot measurements of advanced SiGe:C HBTs are used to examine the characteristics of the transistor in pre-irradiation and post-irradiation. Fig. 7 presents the Ic-Vce and Gummel measurement setup, which consists of the precision semiconductor parameter analyzer and my DUT in common emitter configuration.

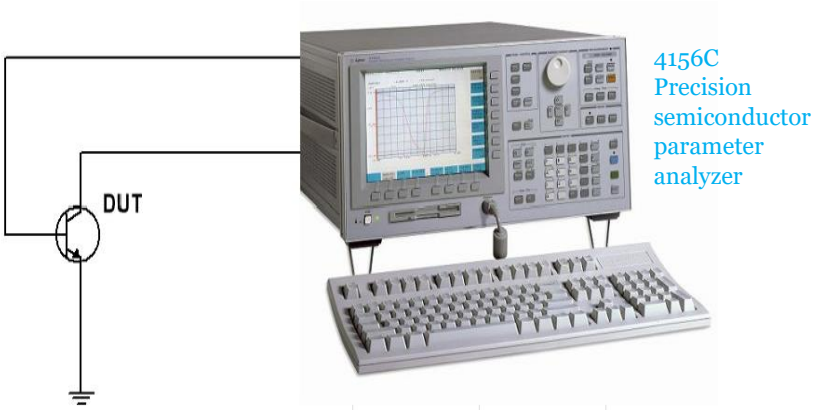

Fig. 7 Gummel and Ic-Vce Measurement setup

2.3 LFN Measurement

LFN measurement is a sensitive measurement technique that needs a special experimental setup to record the power spectral density of noise and reduce the measurement time. The schematic circuit diagram of the LFN measurement system as shown in Fig. 8 consists of the device under test (DUT), biasing circuits, preamplifiers (EG & G 5182), dynamic spectrum analyzer (HP89410A), and computer. Single-finger DUTs are probed by coplanar probes [49] and establish a common emitter configuration. Basing circuits are used to deliver a constant current or voltage to the collector and base terminals. As we exclusively focus on the spectral densities of the base current, the collector-emitter voltage is kept near 0.8 V. And four base current (50 nA, 100 nA, 200 nA, & 500 nA) spectral densities are employed in the investigation for LFN measurements.

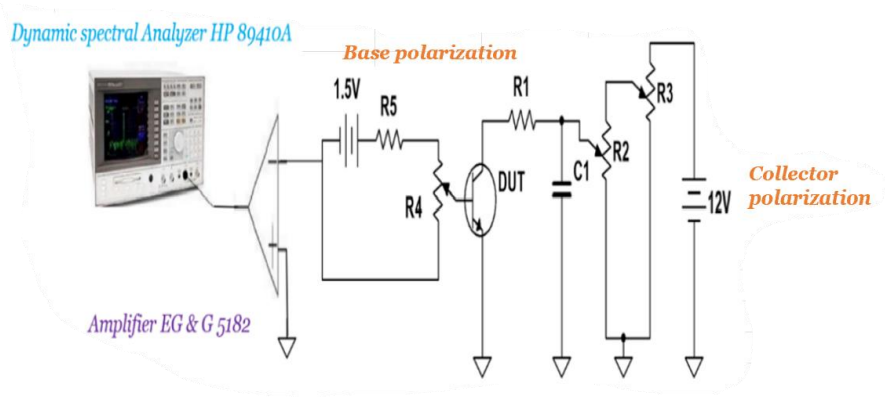

Fig. 8 LFN measurement setup

The low noise transimpedance amplifier (EG & G 5182) is used to detect the small base current noise and amplify the resulting noise signal. Subsequently, the amplified noise signal is recorded and analyzed by a dynamic spectrum analyzer (HP89410A). To eliminate disturbance or interference, all the equipment except the dynamic spectrum analyzer is placed in a Faraday cage. Finally, a base current noise spectral density will be collected by the computer, and further analysis will be done on the data. The same steps are repeated for each base current.

2.4 Radiation source

The irradiation experiments were conducted by utilizing a 320 keV X-ray generator source from the PRESERVE platform located at the Institute of Electronics and Systems (IES), the University of Montpellier. A parallel transmission chamber calibrated in air with a spectral range of 7.5 keV to 320 keV was used to monitor the dose. The X-ray irradiation source and SiGe:C HBT sample are shown in Fig. 9.

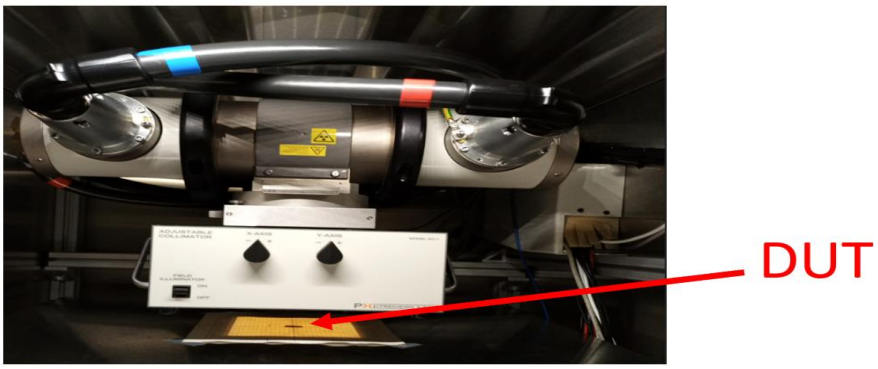

.

Fig. 9 Image of the X-ray irradiation chamber source

2.4.1 Experiments on irradiation

The x-ray irradiation experiment was performed on three samples of the same B55 wafers in two campaigns. The first campaign was done on sample #1 and sample #2 at dose rates of 13.333 rad(air)/sec and 11.333 rad(air)/sec respectively. Sample #1 was irradiated without aluminum filter, whereas sample #2 was irradiated with 2mm aluminum filter. Both experiments were done in 7 steps with a dose of 40 krad(air) until it reached a maximum TID of 280 krad(air), and each step was interrupted for 40 minutes to perform DC characterization. A total of 24 HBTs with an emitter area range of 1 μm^2 to 4.3 μm^2 were used. The first irradiation campaign methodologies are summarized in Table.4 and Table 5

The objective of the first campaign is twofold. Firstly, to determine dose and dose rate in the x-ray irradiation chamber (PTW TM7862), it is necessary to remove low energy photons by implementing filter irradiation [50]. This approach enables a comparison of the results obtained with prior publications, as dose and dose rate are well-established under filter irradiation, unlike without filter radiation. Secondly, the team with whom I am currently collaborating for my master's thesis has already published their research on the effects of TID on SiGe HBTs. Nevertheless, they utilized x-ray irradiation without a filter with a maximum TID of 151 krad (air) [40]. As a result, to facilitate a compressive comparison of my respective results and gain deeper understanding of the dose effects, it is essential to increase the maximum TID to 280 krad(air) in my study.

After the final irradiation, the weekly responses were characterized for four weeks to compare the response with the TID of 280 krad(air) and to examine the possible recovery mechanism at room temperature. During the fifth week, the second irradiation campaign was performed on two samples, namely sample #2 (i.e., a sample that had already been irradiated with a TID of 280 krad(air) by 2 mm Al filter irradiation in the first campaign) and sample #3 (i.e., a new sample for LFN measurement), by using 2 mm aluminum (Al) filter irradiation. The aim of the second campaign is to extend the irradiation dose of sample # 2 from a TID of 280 krad (air) while at the same time irradiating the new sample (sample #3). The experiment was done in six steps at a dose of 40 krad(air) and a dose rate of 11.333 rad(air)/sec. Between each irradiation step,

three hours were allotted for DC and LFN characterization. Tables 4, 5, and 6 summarize the x-ray radiation methodologies of the first campaign.

The transistors are unbiased during irradiation, and the radiation temperature was held at room temperature.

Samples	Dose rate (rad (air)/sec)	2mm Al Filter
Sample #1	13.333	No
Sample #2	11.333	Yes
Sample #3	11.333	Yes

Table 4 Dose rate and type of irradiation specifications

steps	Dose (krad (air))	TID (krad(air)) on sample #1	TID (krad(air)) on sample #2
1	40	40	40
2	40	80	80
3	40	120	120
4	40	160	160
5	40	200	200
6	40	240	240
7	40	280	280

Table 5 Irradiation methodologies for first campaign

steps	Dose (krad (air))	TID (krad(air)) on sample #2	TID (krad(air)) on sample #3
1	40	320	40
2	40	360	80
3	40	400	120
4	40	440	160
5	40	480	200
6	40	520	240

Table 6 Irradiation methodologies for second campaign

2.4.2 Annealing measurements

After sample #1 and sample #2 were irradiated with a maximum TID of 280 krad (air) and 520 krad (air) respectively, and the weekly responses were investigated for 10 weeks and 5 weeks, annealing experiments were conducted on both samples at 100 ℃ and 130 ℃ to examine the possible recovery mechanisms. Table 7 summarizes the annealing methodologies.

Baking Temperature (℃)	Baking hours	Samples
100	100	sample #1
	68	sample #2
130	24	
	90	

Table 7 Annealing methodologies.

Chapter 3. Results and Discussions

As LFN can upconvert to high frequency in integrated circuits due to the nonlinearity of electronic devices, it is important to characterize and model LFN. The radiation-rich environment causes significant effects on electronic devices. It reduces the performance and reliability of electronic devices. Therefore, it is crucial to conduct adequate characterization of electronics devices under irradiation to ensure the proper functionality of the device in the radiation environment.

As such, to measure and model the LFN of HBTs and examine the effects of irradiation on the DC characteristics and LFN of HBTs, it is necessary to start with the DC characteristics of pristine devices. Section 3.1 aims to present the DC characteristics of pristine 55 nm SiGe: C advanced HBTs. The DC characteristics of HS, MV, and HV pristine HBTs will be compared. Section 3.2 will present the LFN characterization and modeling of pristine HBTs. Three types of noise were examined. The 1/f noise and g-r noise of pristine HBTs with different geometries will be compared, and the SPICE parameters will be used to model the LFN. Section 3.3 will discuss the impacts of x-ray irradiation on DC characteristics. Additionally, to test the effect of time on a possible recovery process, the findings from weekly measurements will also be presented. Section 3.4 will present the impacts of x-ray irradiation on the LFN of B55 technologies. And finally, the result of the annealing experiments, which were done at 100 ℃ and 130 ℃, will be presented in Section 3.5.

3.1 DC characterization of pristine devices.

As explained in Section 2.2, DC characterization (Gummel plot and Ic-Vce plot) was performed to study the static characteristics of HBTs. The objective of this characterization is to understand the basic static characteristics of pristine devices and to determine the range of biasing current or voltage used for LFN measurements. DC measurements were investigated on selected HBT devices with an emitter area range of 1 to 4.2 μm^2 in two ways: 1) Gummel plot, and 2) Ic-Vce characterization.

3.1.1 Gummel plot measurements

The selected pristine HBTs are biased in the common emitter configuration, as shown in Fig. 7. The base and collector currents can be expressed as:

$$Ib = Isbe^{\frac{qVbe}{\eta bkT}} \tag{13}$$

$$Ic = Isce^{\frac{qVbe}{\eta c\, kT}} \tag{14}$$

where q is the charge of an electron, Isb is the base saturation current, Isc is the collector saturation current, and ηb and ηc are the ideality factors of the base and collector current, respectively.

The current gain, hFE, is given by:

$$hFE = \frac{Ic}{Ib} \tag{15}$$

The three HBTs, HS, MV, and HV, have different selectively implanted collector (SIC) doping. For instance, HS transistors have higher SIC doping than MV and HV transistors. The lowest SIC doping is that of the HV transistors. This SIC doping variation affects the breakdown voltage of transistors as well as their high-frequency performances, as summarized in Table 2.

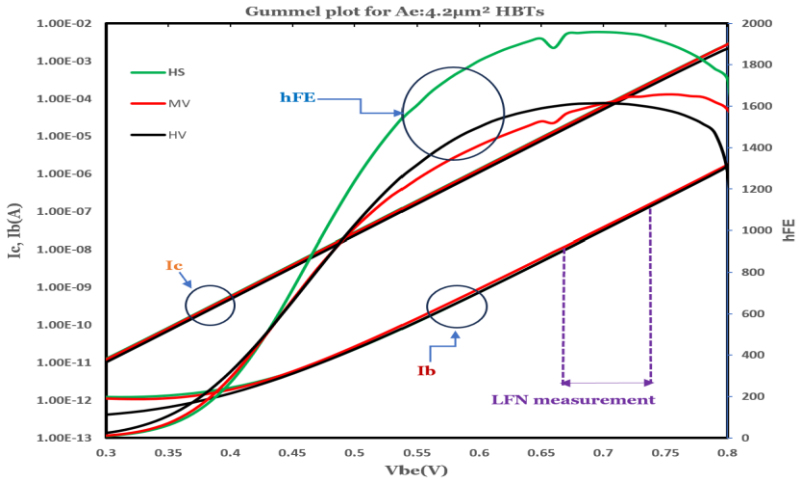

Fig. 10 Forward Gummel plot three HBTs of 4.2 μm^2.

As depicted in Fig. 10, the three flavors present the same collector current, unlike their base current in a low injection regime or Vbe close to 0.4V. For Vbe < 0.4V, the tunneling current of HS and MV transistors is greater than that of HV transistors. This is believed to be related to the doping of SIC. SIC doping also affects the current gain of HBTs, which is clearly observed in Fig. 10, which leads HS transistors to record the highest current gain (i.e., hFE ≈ 1900) compared to the other two flavors (i.e., hFE ≈ 1600). The high current gain of the HS transistors leads to HS transistors operating at the maximum oscillating frequency, fmax, and cutoff frequency, fc, as presented in Table 2.

To investigate LFN and radiation effects in sections 3.2 and 3.3, respectively, it will be necessary to first understand the base current components. The base current has four current components at different Vbe ranges: 1) tunnel current, 2) generation and recombination (g-r) current, 3) diffusion current [51], and 4) high injection-region current. For Vbe less than 0.45V, the tunnel current and generation recombination currents dominate the base current. On the other side, the high injection dominates for Vbe greater than.8 V, and in the middle range for 0.45 V < Vbe < 0.8 V, the diffusion component dominates the base current. Therefore, the experimental base current can be modeled by:

$$Ib = A * Vbe(Vm - Vbe)^2 + Ibo2\, e^{\left(\frac{qVbe}{\eta g-r\, kT} - 1\right)} + Ibo1\, e^{\left(\frac{qVbe}{\eta df\, kT} - 1\right)} \qquad (16)$$

where A is constant in A/V^3, Vm is constant voltage in V, $\eta g - r$ and ηdf are generation-recombination and diffusion ideality factors, respectively, Ibo1 is the diffusion saturated current, and Ibo2 is the generation and recombination saturated current. The first

component is tunnel base current, the second component is g-r base current, and the third component is diffusion base current.

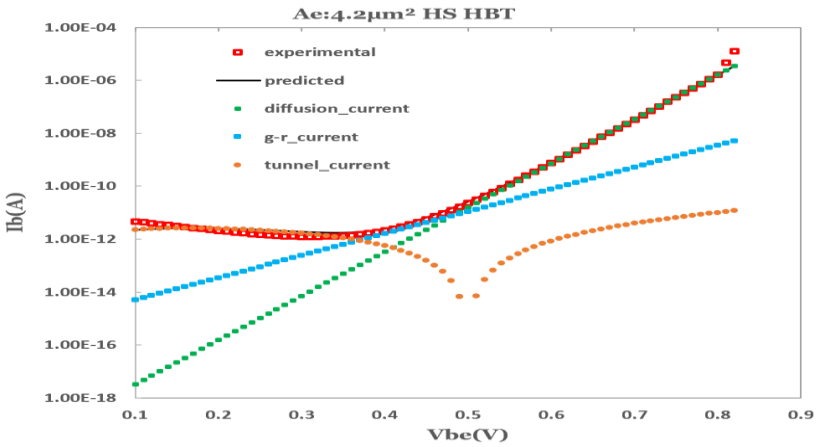

Fig. 11 Base current components.

The experimental base current is modeled by the fitting parameter values ηdf=1, ηg – r = 2, Vm = 0.5 V, A =1.4 $\times 10^{-10}$ A/V^3, Ibo2 =2 $\times$ 10^{-15} A and Ibo1 =1.9 $\times$ 10^{-19} A as presented in Fig. 11.

3.1.2 Ic-Vce characterization

The Ic-Vce plot of an HBT with an emitter area of 2.1 μm² is presented in Fig. 12 for HS, MV, and HV transistors. The measurements were performed at base currents of 200 nA, 400 nA, 600 nA, and 800 nA. At the same Ib and Vce, the HS HBTs have the highest collector current than the MV and HV HBTs, whereas the HV HBTs have the lowest collector current, and the MV HBTs have a medium collector current.

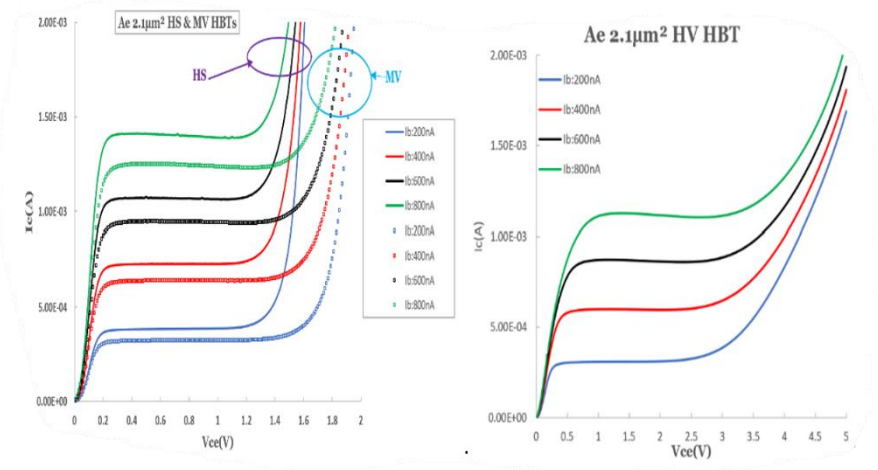

Fig. 12 Ic vs Vce plot for 2.1 μm² HS and MV HBTs (left) and HV HBT(right)

However, in terms of breakdown voltage, HV HBTs have the highest breakdown voltage approximately close to 3 V, whereas HS HBTs have the lowest breakdown voltage close to 1.4 V [38]. This is the trade-off between breakdown voltage and speed.

3.2 LFN Spectral Analysis of pristine devices

Apart from the complexity and time-consuming nature of LFN measurement, the basic characteristics of each noise component have to be investigated. I did the spectral measurement from 10 Hz to 100 kHz, which may have three noise components: 1/f noise, shot noise, and/or generation-recombination (g-r) noise. The LFN spectral density is modeled as:

$$\mathrm{Sib} = \frac{B}{f} + \sum_i \frac{Ai}{1+(\frac{f}{fci})^2} + 2qI_b \qquad (17)$$

where the first component is 1/f noise, the second component is g-r noise, and the third component is shot noise. The shot noise is dominant above 1 kHz. But in the case of 1/f noise and g-r noise, it is not always true that both components appear in the spectrum as 1/f noise can sometimes be masked by one or two g-r components, as can be seen in Fig. 13.

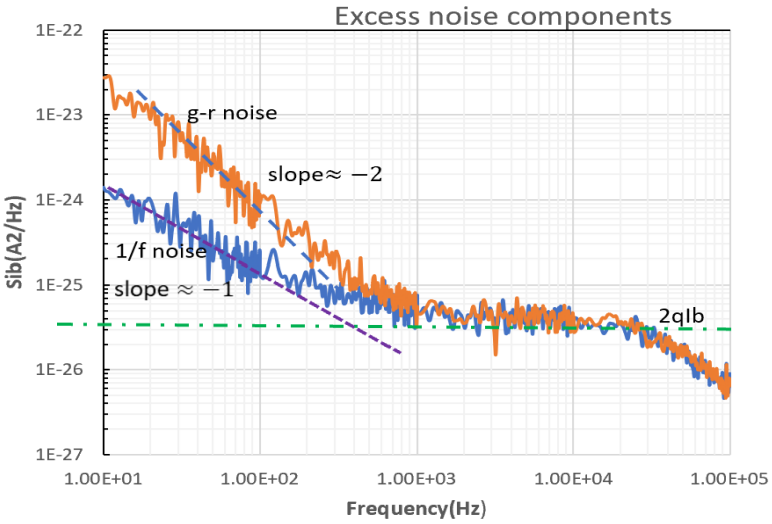

Fig. 13 Sib of 1/f noise, g-r noise and shot noise

In order to explore the LFN, a total of 48 transistors with emitter areas of 1, 2, 3, and 4.2 μm² were used. Three flavors of SiGe:C HBT (HS, MV, and HV) were also included to study the effects of SIC doping on LFN. Each transistor's Sib at 50 nA, 100 nA, 200 nA, and 500 nA was examined.

The Sib shown in Fig. 14 is for the Ae of 2 μm^2 SiGe HBTs (HS, MV, and HV). While g-r noise dominates in HV and 1/f noise dominates in HS and MV transistors, due to the dispression that El Beyrouthy J. [52] has investigated, this may not be true for transistors with different wafer transistors or samples.

The LFN measurement conducted for four input base currents in Fig. 14 revealed the dominant noise to be 1/f noise. Additionally, the level of Sib increases with the base current.

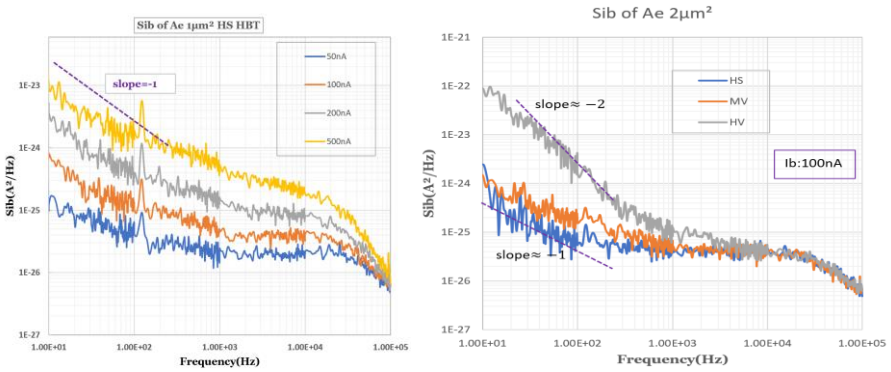

Fig. 14 Sib of Ae=1μm²HS HBT for four currents(left), and Sib of HS, MV and HV for 2 μm² at Ib of 100nA(right).

3.2.1 1/f Noise Analysis

Upon identification of a LFN spectrum having 1/f noise and shot noise in different devices, the modeling of 1/f noise is achieved through the relation (10). As a result, the SPICE parameters, namely (γ, Af & Kf) are extracted. The detailed procedure for the extraction of SPICE parameters is elaborated in Section 1.5.1.

Fig. 15 presents Sib of 1/f noise at 1Hz for two emitter area transistors (2 μm² & 3 μm²) for four Ib. The results illustrate that the 1/f noise at 1 Hz appears to be equal for the three collector structures. Moreover, the 1/f noise demonstrates a quadratic dependence with Ib for both HBTs independent of collector structure [38]. As the 1/f noise exhibits the quadratic law in the presence of Ib, the derivation of Kf can be achieved through relation (11) and subsequently plotted versus the emitter area in Fig. 16.

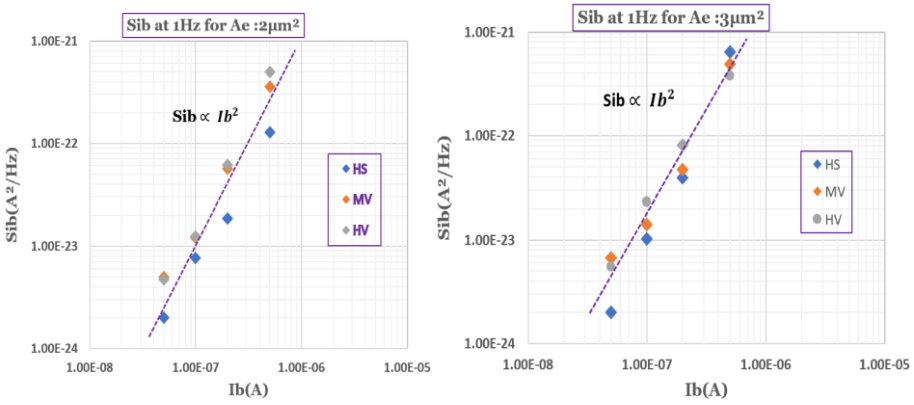

Fig. 15 Sib of 1/f noise at 1Hz of 2 μm^2 (left) and 3 μm^2 (right) HBTs

Since the 1/f noise Sib demonstrates Ib² proportionality and inverse proportionality with Ae in Fig. 16, it is of utmost importance to establish a figure of merit, Kb. This figure of merit enables me to effectively compare the 1/f noise performance of a 55 nm HBT with other transistors. Thus, the mean value of Kb at 1 μm² as obtained via a relation (18) approximates to 3×10^{-9} μm², a result that is greater than the findings of [38].

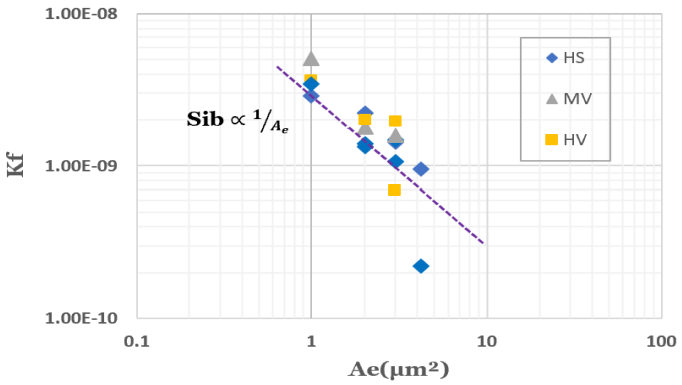

Fig. 16 Kf with Ae for HS, MV and HV HBTs.

$$K_B = K_f . A_e \tag{18}$$

The evolution of Sib at 1 Hz in relation to emitter perimeter-emitter area ratio, Pe/Ae, for three collector structures (HS, MV, and HV) while considering four input base currents is plotted for selected HBTs in Fig. 17. And it is evident that Pe/Ae has a negligible impact on the evolution of Sib at 1 Hz [32], [33].

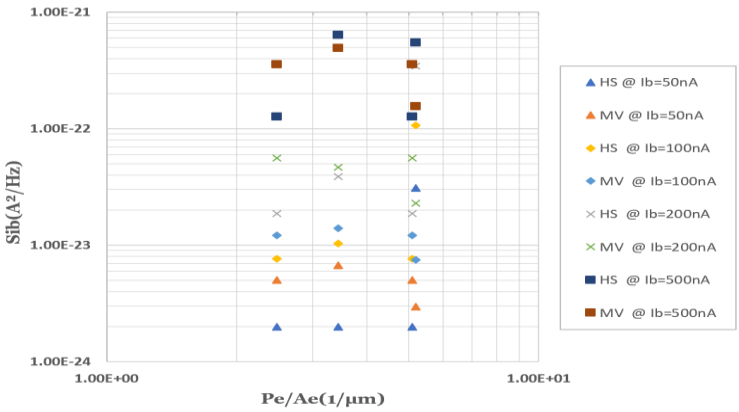

Fig. 17 Sib with function Pe/Ae for HS & MV HBTs at four Ib.

Sib is directly proportional to Ib^2 and inversely proportional to Ae, combined with the negligible dependence on Pe/Ae, resulting in the uniform distribution of 1/f noise sources in the emitter area [27], [28], [53] of SiGe HBTs rather than being concentrated in the emitter periphery. Additionally, the insignificant impact of collector doping on 1/f noise supports the idea that the emitter-base (E-B) area is the possible physical location of the 1/f noise source in comparison to the collector-base (C-B) area [54].

3.2.2 G-r noise Analysis

Unlike ordinary BJT transistors, advanced SiGe:C HBTs are influenced by the g-r noise. This is also demonstrated at two technology nodes of BiCMOS, namely 55 nm and 130 nm [52]. The investigation of g-r noise needs statistical study, and it was determined that the presence of g-r noise in B55 technology is approximately 70 percent.

The analysis of the g-r noise component will be presented in this section. The presence of g-r noise in the device is identified by the Lorentzian shaped spectrum after the data is retrieved onto the computer. The Lorentzian-shaped spectrum is characterized by a magnitude (Plateau) and cutoff frequency, as explained in Section 1.5.2. The extraction methods of g-r noise and its compact modeling will be presented in the subsequent paragraphs.

The compact modeling of two g-r noise components with a Lorentzian-shaped spectrum is presented as:

$$S_{Ib-gr} = \frac{A_1}{\left(1+\frac{f}{f_{c1}}\right)^2} + \frac{A_2}{\left(1+\frac{f}{f_{c2}}\right)^2} \tag{19}$$

where (A_1, A_2) and (f_{c1}, f_{c2}) are plateau and cutoff frequencies of g-r noise components. The subscripts 1 and 2 represent the first and second g-r components, respectively.

The g-r noise parameters were extracted using a developed MATLAB software interface after I took a training with the developer, Prof. Alain Hoffmann. Fig. 18 shows a sample of two g-r noise parameters that were extracted from the MATLAB software interface. The extracted values demonstrate that the parameters for $2.82 \times 10^{-22}\ A^2/Hz$, 7.36 Hz) and ($1.97 \times 10^{-24}\ A^2/Hz$, 562.8 Hz) correspond to (A_1, f_{c1}) and (A_2, f_{c2}) respectively.

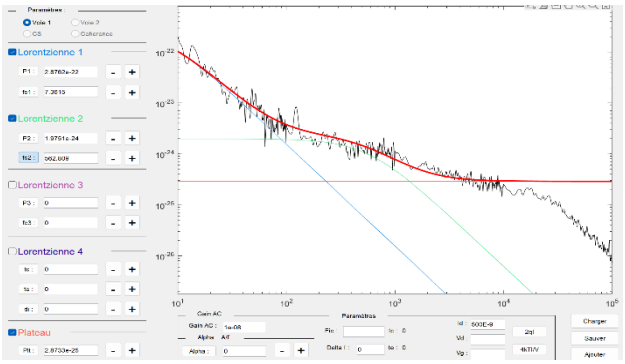

Fig. 18 G-r noise parameter extraction by using MATLAB software interface.

Publications have shown that the possible physical location of g-r noise is the emitter-base region near the space charge region [32]. And this is also in line with the results found by correlation measurements [55]-[57]. A few works suggest that the emitter-base periphery is the physical location of the g-r noise [58].

By following a similar approach as that of [29], the relationship of plateau, Ai with input base current and emitter geometries will be investigated, which will enable us to locate the g-r noise source. This study was done on four Ae HBTs, specifically 1 µm², 2 µm², 3 µm², and 4.2 µm². As it is depicted in Fig. 19, unlike 1/f noise, the plateau level, A1, of g-r noise with respect to emitter area, Ae, is negligible independent of Ib. This result is consistent with the prior findings [29], except for the current bias.

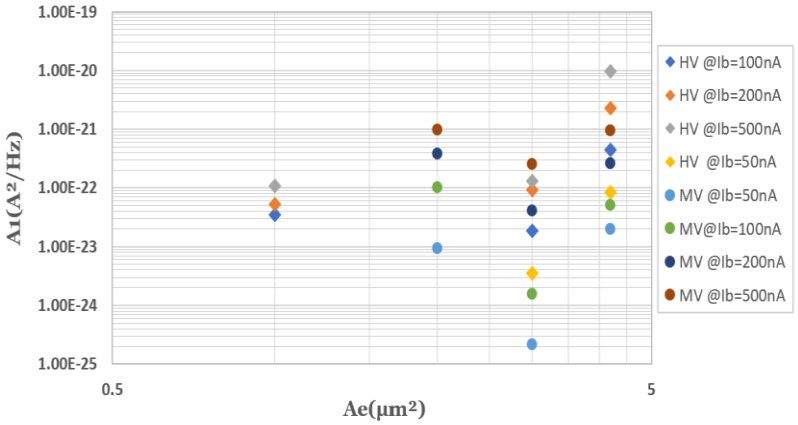

Fig. 19 A_1 with function of A_e for 50 nA,100 nA, 200nA & 500 nA

Fig. 20 illustrates the impact of Pe/Ae on A1/Ae for three HS and HV HBTs. The A1/Ae decreases with respect to Pe/Ae in Ib of 100 nA, 200 nA, and 500 nA.

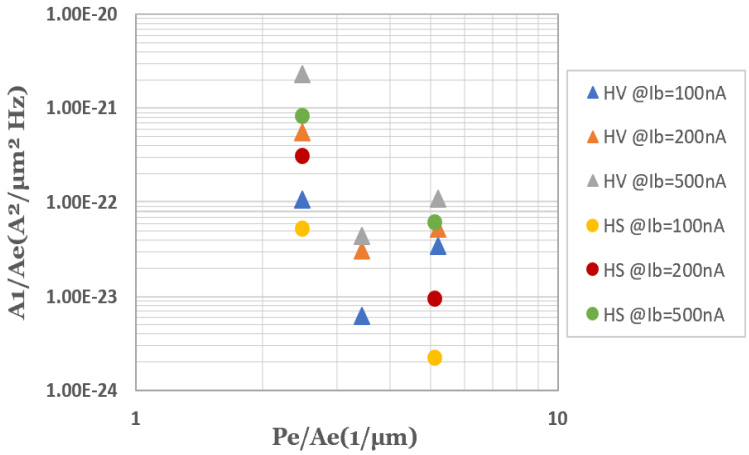

Fig. 20 A1/Ae with function of Pe/Ae for Ib of 100 nA, 200 nA & 500 nA .

Since the contribution of the Ae on A1 is negligible regardless of I b, the emitter periphery is the possible origin of the g-r noise sources. To probe further, A1 is plotted with bias current in Fig. 21 for three Ae HBTs.

As clearly shown in Fig. 21, it is evident that A1 has a quadratic dependence on Ib ($A1 \propto Ib^2$) for 2 µm² HS, 3 µm² HV, 4.2 µm² HS, MV and HV transistors.

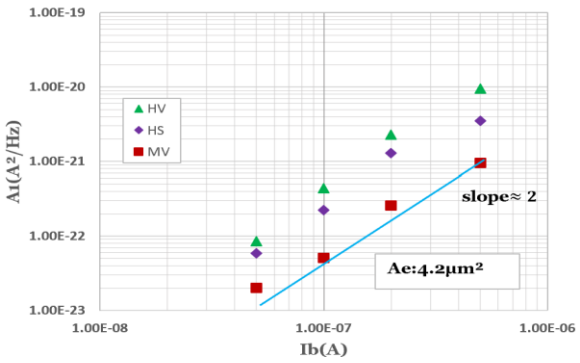

(a)

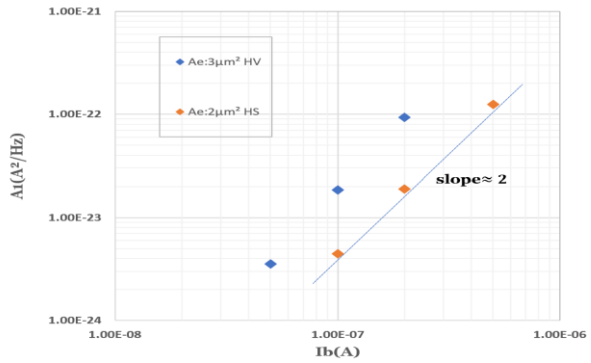

(b)

Fig. 21 A1 with function of Ib for (a) 2μm and (b) 3 μm².and 4.2 μm² HBTs.

By combining the inverse Pe relationship and the quadratic Ib relationship of A1, a model is presented as:

$$A_1 = K_{g-r}\frac{Ib^2}{P_e} \tag{20}$$

In addition to Ib^2 dependence and independence with an Ae of plateau (A1), g-r noise exhibits an inverse Pe dependence. Thus, the possible physical location of g-r noise source is the periphery of the emitter [29], [32], [56], specifically the SiO_2/emitter-base space charge region.

3.3 DC characteristics of irradiated HBTs

The forward Gummel mode response of HBT with an emitter area of 4.2 μm² is presented after each irradiation step with 2 mm aluminum filter x-ray irradiation. As it is presented in Fig. 22, the irradiation response is plotted with Ib, Ic, and current gain (hFE). Unlike the collector current (i.e., the pre-irradiation and post-irradiation collector currents coincide), the base current increases with irradiation. This increases the base current, which subsequently results in current gain degradation.

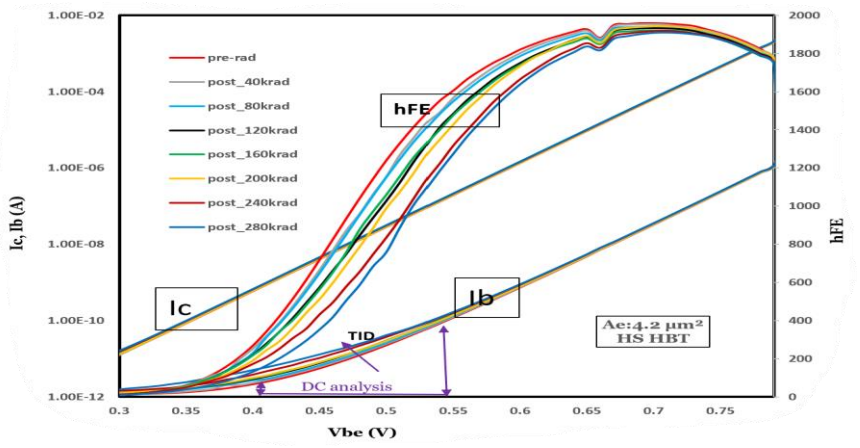

Fig. 22 X-ray Irradiation response of HS HBT with an Ae =4.2 µm².

To provide further insight, the normalized base and collector currents are plotted as a function of the base-emitter voltage Vbe. The normalized base and collector are expressed in relations (21) and (22) as:

$$\frac{\Delta ib}{ib} = \frac{Ib_{post-irr} - Ib_{pre-irr}}{Ib_{pre-irr}} \quad (21)$$

$$\frac{\Delta ic}{ic} = \frac{Ic_{post-irr} - Ic_{pre-irr}}{Ic_{pre-irr}} \quad (22)$$

These equations help to understand the effects of x-ray irradiation quantitatively by comparing the post-irradiation and pre-irradiation currents.

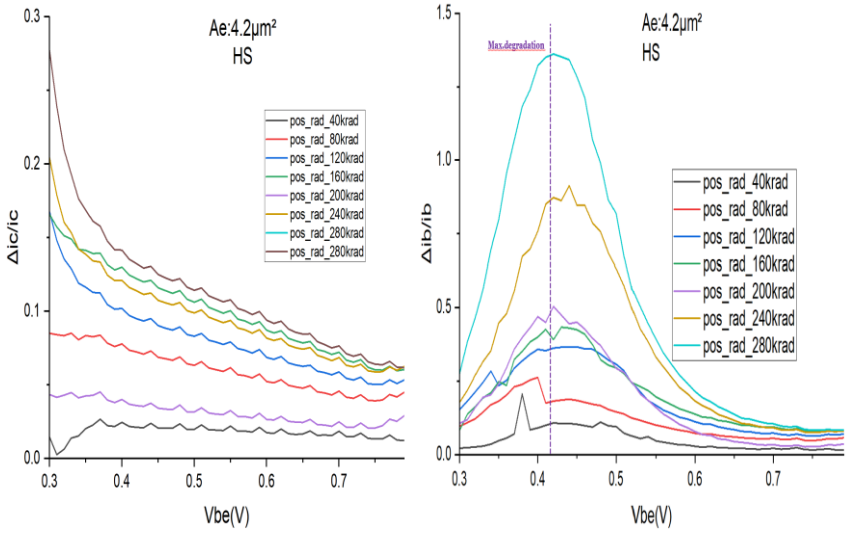

Fig. 23 Δic/ic (left) and Δib/ib(right) with function of Vbe for Ae =4.2 µm² HS HBT.

The collector current, as illustrated in Fig. 23, exhibits a negligible impact from radiation, as evidenced by its maximum Δic/ic value remaining close to 0.15 despite TID. On the other hand, the base current shows an increase with radiation dose, with

maximum increases Δib/ib of approximately 1.25 observed at 280 krad (air) and 0.4 V. Furthermore, the low injection region (i.e., 0.3 V < Vbe < 0.6 V) exhibits an increase in base current, which corresponds to the base current generation-recombination (g-r) component, as presented in Section 3.1.

To gain a deeper understanding of the effects of TID on Ib components, I applied a fitting technique to the experimental data using equation (16). The resulting plot, as seen in Fig. 24, displays the sample experimental data alongside the predicted plot. To depict each irradiation step, the fitting parameter values are recorded in Table 8.

The graph in Fig. 24 demonstrates the excellent fit between the predicted (modeled) plot and the experimental data plot. Unlike the diffusion base current components, the g-r and tunnel base current components show a significant increase near Vbe of 0.4 V.

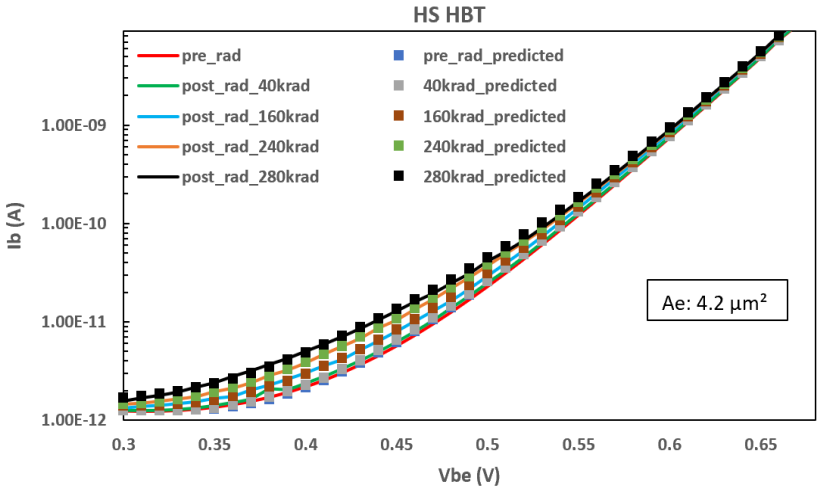

Fig. 24 Experimental and predicted plot with Vbe for Ae =4.2 µm² HS.

Table 8 reveals that the high increases due to TID are recorded in the Ibo2, g-r base current components. But the diffusion base current component doesn't show significant increases. Therefore, the increase in base current due to TID is attributed to the increase in the g-r and tunnel base current components [59]. Due to the difficulty in controlling and investigating the tunnel base component, my focus will solely be on the g-r base current component.

Radiation steps	Ibo1 (A)	Ibo2 (A)	A (A/V³)	Vm (V)
Pre-irr	$1.9x10^{-19}$	$1.8x10^{-16}$	$8.8x10^{-12}$	0.5
40 krad(air)	$1.9x10^{-19}$	$2.2x10^{-16}$	$8.8x10^{-12}$	0.5
80 krad(air)	$1.9x10^{-19}$	$2.5x10^{-16}$	$8.8x10^{-12}$	0.5
120 krad(air)	$1.9x10^{-19}$	$2.8x10^{-16}$	$8.8x10^{-12}$	0.5
160 krad(air)	$1.9x10^{-19}$	$3x10^{-16}$	$8.8x10^{-12}$	0.5
200 krad(air)	$1.9x10^{-19}$	$3.5x10^{-16}$	$8.8x10^{-12}$	0.5
240 krad(air)	$1.905x10^{-19}$	$4x10^{-16}$	$9x10^{-12}$	0.5
280 krad(air)	$1.91x10^{-19}$	$5.2x10^{-16}$	$9.1x10^{-12}$	0.5

Table 8 Fitting parameter values at different TID for 4.2 µm² HS HBT

Let's recall Fig. 5 to understand where the radiation-induced trap centers are located. The radiation-induced trap centers in SiGe HBTs are pedestal trap centers, spacer trap centers, and STI trap centers. Based on publication [46], radiation induces trap centers, which are found in spacer trap centers, which deplete the emitter-base (E-B) junction and increase the base current due to an increase in recombination base current. But the radiation-induced traps created in the shallow trench isolation (STI) and deep trench isolation (DTI) are less responsible for the increase in base current as it is far from the carrier transport of the transistor [1]. In the next section, the impacts of geometry on the radiated device under test will be presented.

3.3.1 Geometry effect

To understand the geometry effect, a comprehensive study was conducted on 12 HBTs from sample #2. First, the normalized base current is plotted as a function of TID for four Ae MV HBTs in Fig. 25. The findings indicate that the impact of geometry is relatively insignificant for TID values less than 120 krad(air) [59]; however, as TID increases, the impact of geometry on base current becomes more pronounced. Consequently, smaller geometry transistors exhibit higher degradation (i.e., close to 3) compared to larger geometry transistors (i.e., close to 0.9) at a maximum TID of 280 krad(air). The HV and HS flavors, although not depicted here, exhibit a similar trend to that of MV HBTs.

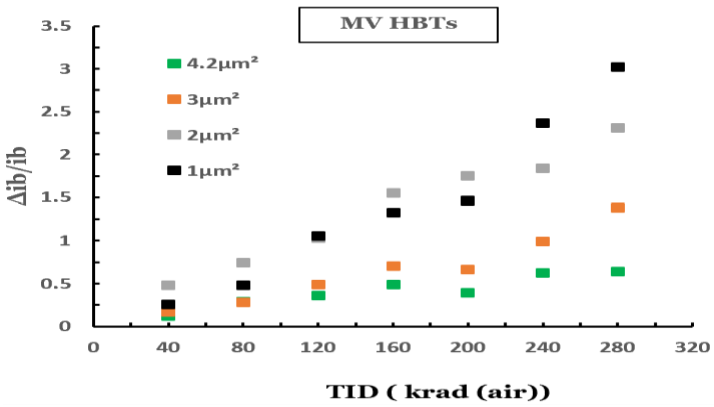

Fig. 25 Plot of Δib/*ib* with TID for four Ae MV HBTs at Vbe=0.54V.

To locate the possible sources of radiation-induced g-r centers, Δib/*ib* is graphed as a function of Pe/Ae and Ae at Vbe = 0.54V and TID of 280 krad(air) for three HBT flavors, as illustrated in Fig. 26. The graph reveals Δib/*ib* increases with Pe/Ae [45], [61], and it has a slope close to 1, whereas Δib/*ib* with a function of Ae has a slope less than -0.6, Hence, based on Fig. 25, I can deduce that the collector structure will not possibly have an impact on the degradation of base current during irradiation in the forward Gummel plot. As a result, the primary source of degradation is found on the E-B geometry side, not on the C-B geometry side. In Fig. 26, Δib/*ib* is plotted with a function of Pe/Ae and Ae which exhibit a slope close to 1 and 0.6, respectively. This reveals that the induced g-r traps are mainly due to the peripheral effect, regardless of the transistor flavor, specifically the E-B spacer oxide [59], [62]. And this is consistent with the work of [1], [44]

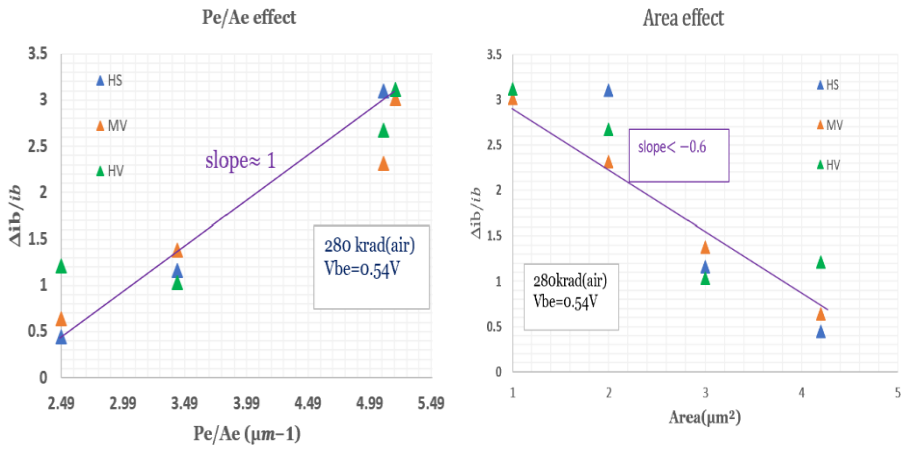

Fig. 26 plot of Δib/ib with Pe/Ae(left) & Ae (right)

Since the base current after irradiation is mainly dependent on the peripherals of the device, it can be expressed as:

$$Ib_{post_{rad}} = Ib_{pre-irr} + P_e J_{bl} \exp\left(\frac{V_{be}}{n_{bg-r} Vt}\right) \quad (23)$$

where Jbl is the leakage current at emitter-edge length in $pA/\mu m$, $n\text{-}b_{g-r}$ is the generation recombination ideality factor, Vt is the thermal voltage, and $Ib_{pre-irr}$ is the base current before irradiation [41].

3.3.2 The impact of a 2mm Aluminum filter X-ray Irradiation

The impact of irradiation due to a 2 mm aluminum filter and without a filter at dose rates of 11.3333 rad(air)/sec and 13.333 rad(air)/sec, respectively, is investigated on samples #2 and sample #1. The purpose of this experiment is to understand the impact of using a 2 mm aluminum filter during irradiation and to compare my results with prior results that were done on the same device (B55 technology) by utilizing x-ray irradiation without a filter.

Fig. 27 illustrates the impact of without filter x-ray irradiation on 3 μm² HBTs. The relative excess base current (Δib/ib) increases with TID, especially at maximum degradation. In prior study [63], the X-ray irradiation without filter at TID of 151 krad(air) and a dose rate of 4.04 rad (air)/sec on the B55 technology shows a Δib/ib close to 0.8, which is consistent with the results plotted in Fig. 27. At Vbe = 0.54 V and a TID of 160 krad (air), Δib/ib is close to 0.8 for my case. In my experiment, the device was exposed to a maximum of 280 krad (air), and I examined the similar trend as Fig. 26 for without a filter x-ray irradiation (not shown here), which can help to locate the radiation-induced trap center sources. But in prior works on this device, the impact of area was negligible due to a lower TID (i.e., 151 krad (air)).

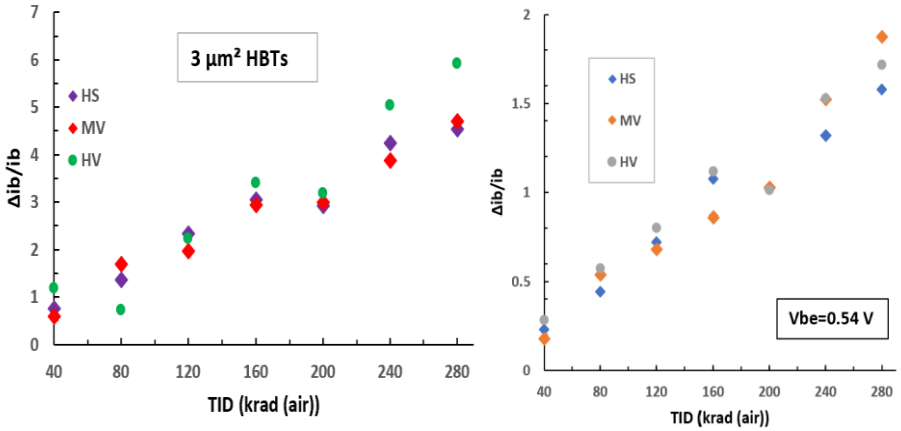

Fig. 27 Δib/*ib* vs TID of without 2mm Al filter by considering maximum degradation (left) and at Vbe=0.54 V (right) for 3 µm² HBTs of sample #1.

In Fig. 28, only HBTs having Ae = 3 µm² from two samples are presented, one of which was irradiated without a filter and the other was irradiated with a 2 mm aluminum filter. The aim of this experiment is to examine the impact of low-energy photons by comparing results with and without filter irradiation (Fig. 28).

The response of HBTs, both with and without 2 mm aluminum filter irradiation, is nearly equal regardless of the irradiation type used. The same trend was investigated for the other emitter-area transistors. In order to reduce the dose rate and measure the dose and dose rate precisely on the ionizing chamber (PTW TM7862), it is necessary to implement with filter irradiation [50]. Therefore, due to the short time, I only use 2 mm aluminum filter irradiations to extend the TID, as will be presented in Section 3.3.4.

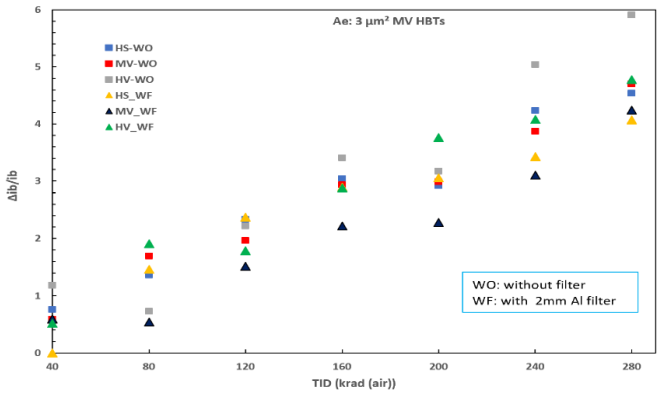

Fig. 28 Δib/*ib* vs TID of with and without 2mm Al filter

Note: WF represents 2 mm aluminum filter radiation, which is plotted by a tringle shape, and WO is without 2 mm aluminum filter radiation, which plotted by a square shape. Here, only maximum degradation is considered for each HBT.

3.3.3 Weekly response

After samples #1 and sample #2 were irradiated with a maximum TID of 280 krad (air), in the first campaign the weekly responses were studied for four weeks on 24 selected

HBTs. The objective of this experiment is to understand the recovery mechanism and examine the impact of time (i.e., post-irradiation time), as well as the measurement time between each irradiation step. To compare the results, the TID response at 280 krad(air) and pre-irradiation is plotted with weekly responses in Fig. 29. And to examine the base current closely, Δib/*ib* is plotted in function of the number of weeks at Vbe of 0.41 V, 0.54 V, and 0.62 V in Fig. 30.

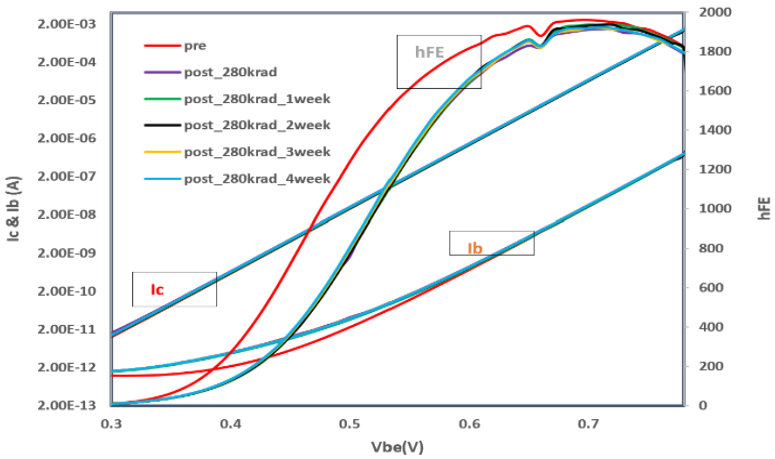

Fig. 29 Weekly response of Ae =4.2 µm² HS HBT

As depicted in Fig. 29, the weekly response (room temperature annealing) is negligible, and this is also clearly shown in Fig. 30, which compares the results at TID of 280 krad(air) with the weekly response on three Vbe voltages. The high degradation at Vbe of 0.41 V is attributed to its location in the g-r region, whereas the other two voltages put the transistor near the diffusion region. V. N. Hegde et al. [59] also demonstrated the negligible impact of room-temperature annealing. In addition, this experiment allows me to conclude that the irradiation response isn't impacted by the measurement time (i.e., the time between each irradiation step). The impact of 10 weeks and a high TID (i.e., 520 krad (air)) on the recovery of DC characteristics at room temperature will be presented in Section 3.5.

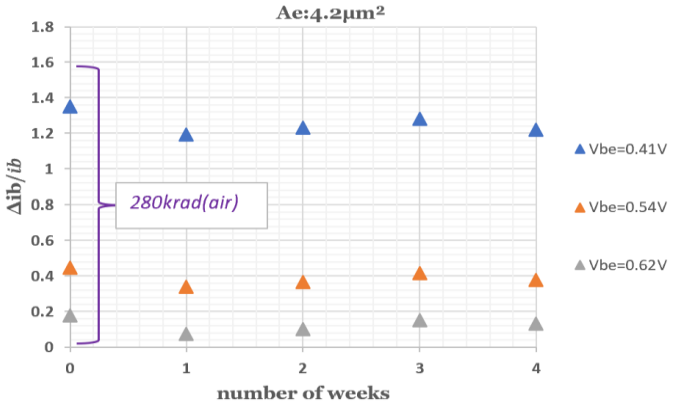

Fig. 30 Weekly response of Ae: =4.2 µm² HS HBT at three Vbe

3.3.4 DC characteristics of SiGe HBTs for TID > 280 krad(air)

The objective of this experiment is to understand and investigate the impact of high TID on advanced HBTs (i.e., TID > 280 krad (air)), as the prior maximum TID on this device was 151 krad (air) [40]. The experiment was done on sample #2 in six steps with a dose of 40 krad (air) at a dose rate of 11.333 rad(air)/sec, as explained in Section 2.4.1. This study was performed on a sample that had already been irradiated with a TID of 280 krad(air) in the first campaign. Between this study and the last irradiation (i.e., TID = 280 krad(air)), there was a four-week interval. And those four-week results are presented in Section 3.3.3.

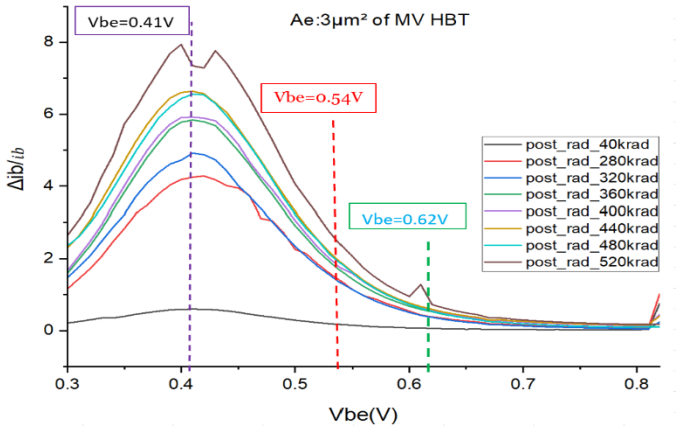

Fig. 31 Δib/*ib* Vs Vbe at different TID for Ae =3μm² MV HBT.

Δib/*ib* is plotted with the function of Vbe at different TIDs, including 40 krad(air) and 280 krad(air) responses for comparison, in Fig. 31. The increase in TID impacts the transistors by increasing the excess (normalized) base current near 8 at 520 krad(air). Notably, the degradation occurs even in the diffusion region, as clearly depicted in Fig. 31. To visualize this phenomenon, Δib/ib is presented with respect to TID at Vbe of 0.41 V, 0.54 V, and 0.62 V in Fig. 32.

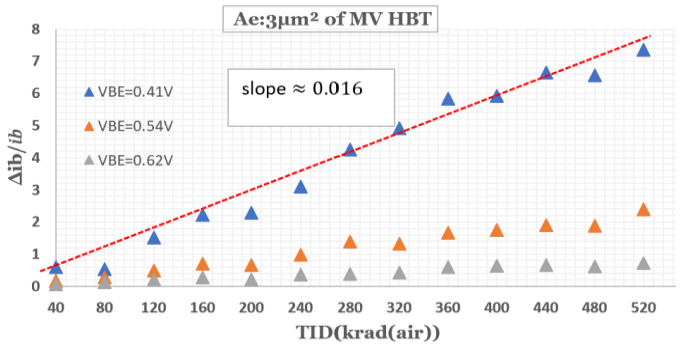

Fig. 32 Δib/*ib* Vs TID at Vbe of 0.41 V, 0.54 V & 0.62 V for Ae = 3 μm² MV HBT.

Fig. 32 shows that Δib/*ib* increases with TID, particularly at Vbe of 0.41 V, which exhibits a slope close to 0.016. Furthermore, Δib/*ib* at Vbe of 0.54 V starts to increase after 200 krad(air). This finding supports Table 8, which indicates an increase in the diffusion base current component after 200 krad(air). The same trend is observed in

other geometric transistors. The result also shows that device (B55 technology) can stand a TID of 520 krad(air).

3.4 Impacts of Irradiation on LFN

The objective of this experiment is to study the impacts of x-ray irradiation on the LFN of SiGe:C HBTs. The experiment was done on sample #3 in six steps with a dose of 40 krad(air) at a dose rate of 11.333 rad(air)/sec, as explained in Section 2.4.1. To make sure the measurements were not performed within the g-r low injection regime and oscillation region, LFN measurements were examined on Ib of 50 nA, 100 nA, 200 nA, and 500 nA, as shown in Fig. 33.

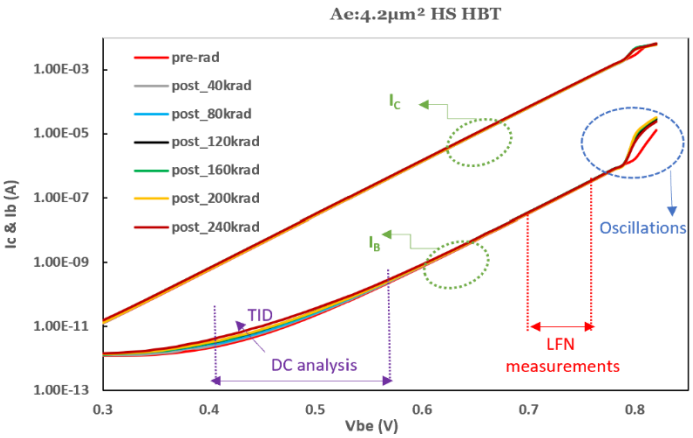

Fig. 33 Gummel plot characteristics of Ae = 4.2 µm² HS HBT

3.4.1 Spectral analysis

As has been presented in Section 3.2, LFN spectra can be described by two main characteristics: the 1/f and shot noise components and the presence or absence of g-r noise [64]. After irradiation, depending on several parameters (TID, bias current, geometry), many behaviors have been observed, making LFN analysis quite complex. For instance, Fig. 34 presents a 2 µm² HS HBT's noise spectra at different doses for Ib of 500 nA. The g-r noise component signatures (cut-off frequency of around 10 Hz and plateau level) present an independent response to irradiation in this case.

Fig. 34 Sib at Ib=500 nA for different irradiation dose on Ae=2 µm² HS HBT.

A second behavior, as depicted in Fig. 35, is characterized by a 1/f noise presenting a stable level at low TID, generally less than 80 krad (air), followed by a new g-r component with a cut-off frequency around 200 Hz and a plateau that can be very sensitive to irradiations.

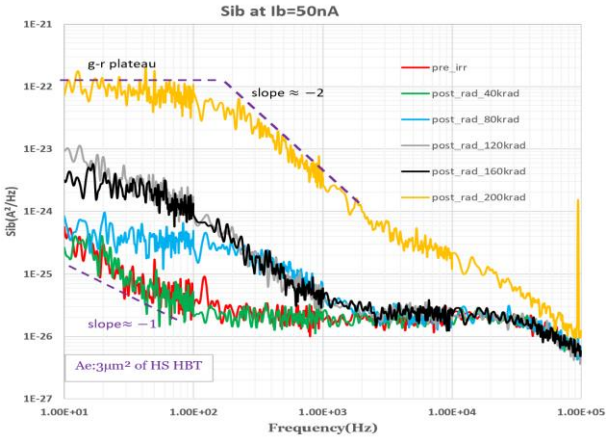

Fig. 35 Sib at 50nA of ib for different irradiation dose on Ae=3μm² HS HBT.

As explained at the beginning of this chapter, LFN measurement is quite complex in addition to being time consuming. It requires a stable measurement setup. During the irradiation experiment, the LFN measurement setup wasn't stable, specifically the collector and base biasing circuits. It was difficult to identify the source of perturbation, as this perturbation could have originated from various sources, namely the basing circuits, wafer pads, coplanar probes, measuring devices (multimeter reading error), or radiation itself. After a few weeks, I could identify the problem, and it was the collector biasing circuit. And then I discussed it with my supervisors about implementing another collector biasing circuit. Although the new collector biasing circuit works well, the LFN experiment and analysis are still ongoing.

3.5 Annealing measurements

Prior studies on this device have shown that annealing at 100 °C after a TID of 151 krad(air) without filter x-ray irradiation has no significant effect on the DC characteristics [65]. Contrary to this, annealing at 100 °C after a maximum TID of 330 krad (air) by using gamma irradiation shows a significant recovery of the device's DC characteristics [66]. The objective of my experiment is to examine the possible recovery of HBTs' DC characteristics at high doses (i.e., 280 krad (air) and 520 krad (air)) and compare $\Delta ib/ib$ of each HBT after annealing.

The details about annealing methodologies are elaborated in Table 7. Before sample # 1 and sample # 2 were baked, the impact of room temperature on the two samples was studied for 10 weeks and 5 weeks, respectively. Fig. 36 presents Δib/ib as a function of Vbe at different annealing times and temperatures for Ae = 3 μm² MV HBT of sample #2.

The results depicted in Fig. 37 show a high recovery of base current, especially after it has been baked at 130 °C for 168 hours. However, the short duration of annealing, for

instance, annealing at 130 °C in 22 hours. shows insignificance in recovery on Δib/*ib* compared to the annealing responses at 100 °C for 168 hours.

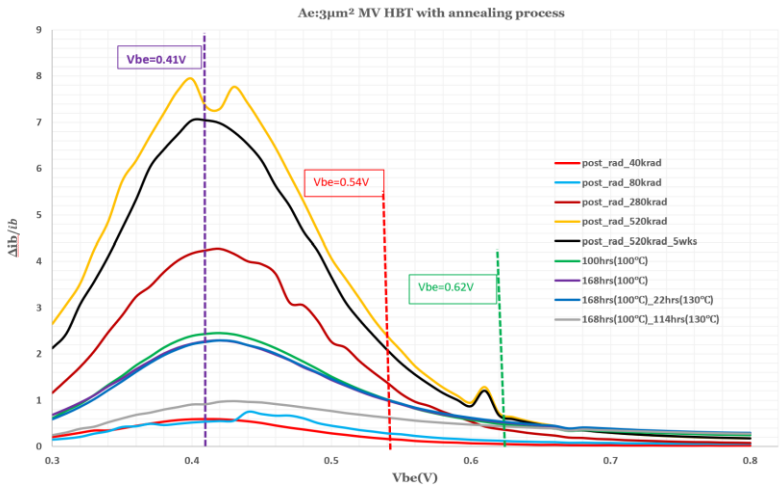

Fig. 36 Δib/*ib* Vs Vbe at different annealing temperature of Ae =3 μm² MV HBT.

In Fig. 37, the Δib/*ib* is plotted with annealing time, and it shows high recovery for both HBTs at Vbe = 0.41 V because at this voltage the base current component is in the g-r region where detrimental effects of radiation happen, as explained in Section 3.3. Moreover, at high temperatures, the induced traps will be released. After 282 hours, both HBTs exhibit nearly equal levels of Δib/*ib* regardless of the maximum TID and Vbe. Unlike the prior study on this device [65], annealing at 100 °C for 168 hours after high TID shows a significant recovery. The work of [47] on 130nm-BiCMOS-8HP shows that annealing at 100 °C after a TID of 1.5 Mrad (SiO_2) has a high recovery on the device characteristics, and this supports my annealing results.

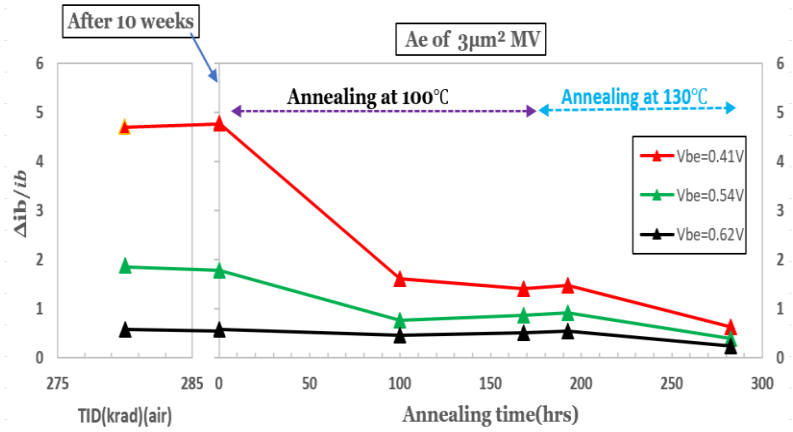

(a)

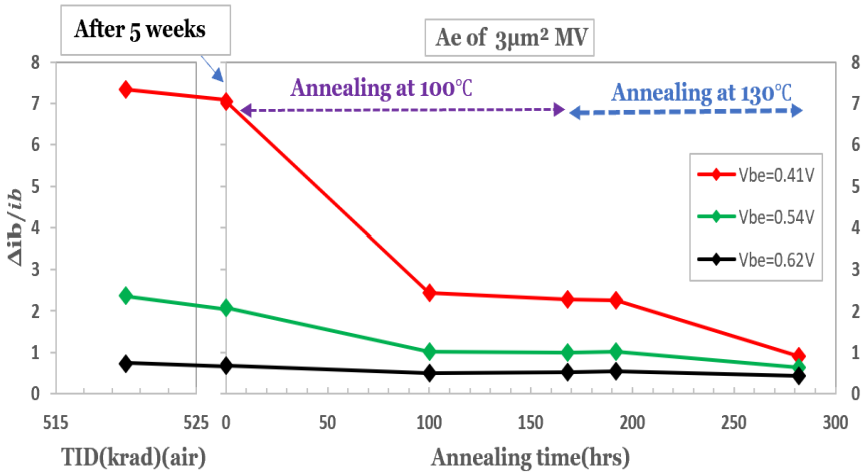

(b)

Fig. 37 Δib/*ib* vs annealing time for 3 μm² MV HBTs on (a) sample #1., and (b) sample#2

Chapter 4. Conclusion and Future Works

4.1 Conclusion

SiGe HBTs have emerged to satisfy the burgeoning demand of wireless communication and high-speed niche applications at a compelling cost advantage. The high integration capability of SiGe technology with CMOS provides a favorable opportunity to leverage the advantages of both technologies. In this thesis, the impacts of x-ray irradiation on the DC characteristics and low-frequency noise of 55 nm advanced SiGe:C HBTs (B55), which exhibit a f_T/f_{Max} of 320/370 GHz and are fabricated by STMicroelectronics, are examined.

The compact SPICE modeling result of the 1/f noise shows that the 1/f noise base current spectral density (Sib) is proportional to the quadratic of base input current and inverse of emitter area, Ae, which results in Kb, a figure of merit representing the 1/f noise amplitude, in the range of 10^{-9} μm². Furthermore, Sib of the device under tests is presented to be independent of emitter perimeter-to-emitter area ratio (Pe/Ae) and collector doping, indicating that the emitter-base area is the possible physical location of the 1/f noise source, which is expected to be uniformly distributed.

Three samples were irradiated to 240 krad(air), 280 krad(air) and 520 krad(air) which is far more than the prior study on this device (i.e., 151 krad (air)). The linear dependence of relative excess base current, $\Delta ib/ib$, with Pe/Ae confirms that the base-emitter periphery is the possible physical location of the radiation-induced trap center sources. This result was not shown in earlier study on this device. The post-irradiation fitting model and the plot of $\Delta ib/ib$ with TID at different emitter-base voltages evidenced that the radiation-induced traps majorly affect the generation-recombination (g-r) base current. Furthermore, the annealing experiment provides clear evidence that the g-r base current recovers more than 85 percent of its increase through radiation. The experimental result explicitly shows that room temperature has negligible impact on the post-irradiation response of SiGe: C HBTs. In general, this thesis's results can provide a significant contribution to the hot research topics of radiation and LFN.

4.2 Future works

As I have tried to explain in chapter 3, LFN measurement is time-consuming and complicated. To investigate the physical location of the noise sources and the impacts of irradiation on LFN, extensive measurements are needed. Furthermore, regarding DC characteristics, our focus was solely on the forward Gummel plot, but it is necessary to perform an inverse Gummel plot and examine the impacts of STI on the base and collector currents. Even though wiring the 55 nm transistor terminals looks difficult, it is necessary to investigate the impacts of biasing during irradiation to ascertain the worst-case degradation scenario. During this thesis, I was unable to cover all the measurements due to a shortage of time and other issues, but all experiments will be initiated on the new ST-Microelectronics HBT, namely B55X, in October 2023.

References

[1] J. D. Cressler, "Radiation Effects in SiGe Technology," in IEEE Transactions on Nuclear Science, vol. 60, no. 3, pp. 1992-2014, June 2013, doi: 10.1109/TNS.2013.2248167.

[2] U. Konig, "SiGe and GaAs as competitive technologies for RF-applications," Proceedings of the 1998 Bipolar/BiCMOS Circuits and Technology Meeting (Cat. No.98CH36198), Minneapolis, MN, USA, 1998, pp. 87-92, doi: 10.1109/BIPOL.1998.741886.

[3] H. Kroemer, "Theory of a Wide-Gap Emitter for Transistors," in Proceedings of the IRE, vol. 45, no. 11, pp. 1535-1537, Nov. 1957, doi: 10.1109/JRPROC.1957.278348.

[4] G. L. Patton, S. S. Iyer, S. L. Delage, S. Tiwari and J. M. C. Stork, "Silicon-germanium base heterojunction bipolar transistors by molecular beam epitaxy," in IEEE Electron Device Letters, vol. 9, no. 4, pp. 165-167, April 1988, doi: 10.1109/55.677.

[5] J. D. Cressler, D. L. Harame, J. H. Comfort, J. M. C. Stork, B. S. Meyerson and T. E. Tice, "Silicon germanium heterojunction bipolar technology: the next leap in silicon?" Proceedings of IEEE International Solid-State Circuits Conference - ISSCC '94, San Francisco, CA, USA, 1994, pp. 24-27, doi: 10.1109/ISSCC.1994.344742.

[6] Jung Han Choi, *High-Speed Devices and Circuits with THz Applications*. CRC Press, 2017. [online]. Available: https://www.oreilly.com/library/view/high-speed-devices-and/9781466590113/xhtml/ch04.xhtml

[7] B. K. Jones, “Electrical noise as a reliability indicator in electronic devices and components,” *IEE Proceedings - Circuits, Devices and Systems*, vol. 149, no. 1, pp. 13–22, Feb. 2002, doi: https://doi.org/10.1049/ip-cds:20020331.

[8] P. Qi, “Low-frequency Noise Power Spectrum Density Characterizing of SiGe HBTs,” pp.32, 2006.

[9] J. D. Cressler and G. Niu, *Silicon-germanium Heterojunction Bipolar Transistors*. Artech House, pp. 263-264, 2003.

[10] B. K. Jones, "Low-frequency noise spectroscopy," in IEEE Transactions on Electron Devices, vol. 41, no. 11, pp. 2188-2197, Nov. 1994, doi: 10.1109/16.333840.

[11] V. Mitin et al., “Generation-Recombination Noise in Semiconductors,” 2002.

[12] F. N. Hooge, "1/f noise sources," in IEEE Transactions on Electron Devices, vol. 41, no. 11, pp. 1926-1935, Nov. 1994, doi: 10.1109/16.333808.

[13] A. L. McWhorter, “1/F Noise and Germanium Surface Properties,” *Semiconductor Surface Physics*. 1957.

[14] J. El Beyrouthy, “Characterization and modeling of low frequencies noise in bipolar transistors developed in BiCMOS technology (55 nm node) for RF to THz applicationsés en technologie BiCMOS (nœud 55 nm) pour des applications RF et THz,” pp.28-29,2020.

[15] M. Sanden, O. Marinov, M. Jamal Deen and M. Ostling, "Modeling the variation of the low-frequency noise in polysilicon emitter bipolar junction transistors," in IEEE Electron Device Letters, vol. 22, no. 5, pp. 242-244, May 2001, doi: 10.1109/55.919242.

[16] M. Sanden, Mikael Östling, O. Marinov, and M. Jamal Deen, "STATISTICAL SIMULATIONS OF THE LOW-FREQUENCY NOISE IN POLYSILICON EMITTER BIPOLAR TRANSISTORS USING A MODEL BASED ON GENERATION-RECOMBINATION CENTERS," *Fluctuation and Noise Letters*, vol. 01, no. 02, pp. L51–L60, Jun. 2001, doi: https://doi.org/10.1142/s0219477501000202

[17] Enhai Zhao et al., "An investigation of low-frequency noise in complementary SiGe HBTs," in IEEE Transactions on Electron Devices, vol. 53, no. 2, pp. 329-338, Feb. 2006, doi: 10.1109/TED.2005.862698.

[18] V. Kumar and W. E. Dahlke, "Low-frequency noise in Cr—SiO2—N-Si tunnel diodes," in IEEE Transactions on Electron Devices, vol. 24, no. 2, pp. 146-153, Feb. 1977, doi: 10.1109/T-ED.1977.18694.

[19] H. A. W. Markus and T. G. M. Kleinpenning, "Low-frequency noise in polysilicon emitter bipolar transistors," in IEEE Transactions on Electron Devices, vol. 42, no. 4, pp. 720-727, April 1995, doi: 10.1109/16.372077.

[20] A. Mounib, G. Ghibaudo, F. Balestra, D. Pogany, A. Chantre, and J. A. Chroboczek, "Low frequency (1/*f*) noise model for the base current in polysilicon emitter bipolar junction transistors," *Journal of Applied Physics*, vol. 79, no. 6, pp. 3330–3336, Mar. 1996, doi: https://doi.org/10.1063/1.361233.

[21] Yiqi Zhuang and Qing Sun, "Correlation between 1/f noise and h/sub FE/ long-term instability in silicon bipolar devices," in IEEE Transactions on Electron Devices, vol. 38, no. 11, pp. 2540-2547, Nov. 1991, doi: 10.1109/16.97420.

[22] O. Jantsch, "Flicker (1/f) noise generated by a random walk of electrons in interfaces," in IEEE Transactions on Electron Devices, vol. 34, no. 5, pp. 1100-1115, May 1987, doi: 10.1109/T-ED.1987.23051.

[23] N. Siabi-Shahrivar, W. Redman-White, P. Ashburn, and H.A. Kemhadjian, "Reduction of noise in polysilicon emitter bipolar transistors," *Solid-state Electronics*, vol. 38, no. 2, pp. 389–400, Feb. 1995, doi: https://doi.org/10.1016/0038-1101(94)00126-z

[24] M. Jamal Deen, J. Ilowski, and P. Yang, "Low frequency noise in polysilicon-emitter bipolar junction transistors," *Journal of Applied Physics*, vol. 77, no. 12, pp. 6278–6288, Jun. 1995, doi: https://doi.org/10.1063/1.359095

[25] G. Niu, "Noise in SiGe HBT RF Technology: Physics, Modeling, and Circuit Implications," in Proceedings of the IEEE, vol. 93, no. 9, pp. 1583-1597, Sept. 2005, doi: 10.1109/JPROC.2005.852226.

[26] Zhenrong Jin et al., "1/f noise in proton irradiated SiGe HBTs," in IEEE Transactions on Nuclear Science, vol. 48, no. 6, pp. 2244-2249, Dec. 2001, doi: 10.1109/23.983203.

[27] J. D. Cressler, L. Vempati, J. A. Babcock, R. C. Jaeger and D. L. Harame, "Low-frequency noise characteristics of UHV/CVD epitaxial Si- and SiGe-base bipolar transistors," in IEEE Electron Device Letters, vol. 17, no. 1, pp. 13-15, Jan. 1996, doi: 10.1109/55.475562.

[28] H. A. W. Markus and T. G. M. Kleinpenning, "Low-frequency noise in polysilicon emitter bipolar transistors," in IEEE Transactions on Electron Devices, vol. 42, no. 4, pp. 720-727, April 1995, doi: 10.1109/16.372077.

[29] C. Mukherjee et al., "Low-Frequency Noise in Advanced SiGe:C HBTs—Part I: Analysis," in IEEE Transactions on Electron Devices, vol. 63, no. 9, pp. 3649-3656, Sept. 2016, doi: 10.1109/TED.2016.2589159.

[30] J. R. Schwank et al., "Radiation Effects in MOS Oxides," in IEEE Transactions on Nuclear Science, vol. 55, no. 4, pp. 1833-1853, Aug. 2008, doi: 10.1109/TNS.2008.2001040.

[31] R. Plana et al., "Low-frequency noise in millimeter-wave Si/SiGe heterojunction bipolar transistors," Proceedings of 1995 IEEE MTT-S International Microwave Symposium, Orlando, FL, USA, 1995, pp. 1431-1434 vol.3, doi: 10.1109/MWSYM.1995.406241.

[32] L. S. Vempati, J. D. Cressler, J. A. Babcock, R. C. Jaeger and D. L. Harame, "Low-frequency noise in UHV/CVD epitaxial Si and SiGe bipolar transistors," in IEEE Journal of Solid-State Circuits, vol. 31, no. 10, pp. 1458-1467, Oct. 1996, doi: 10.1109/4.540056.

[33] L. S. Vempati, J. D. Cressler, J. A. Babcock, R. C. Jaeger and D. L. Harame, "Low-frequency noise in UHV/CVD Si- and SiGe-base bipolar transistors," Proceedings of Bipolar/Bicmos Circuits and Technology Meeting, Minneapolis, MN, USA, 1995, pp. 129-132, doi: 10.1109/BIPOL.1995.493881.

[34] L. Bary et al., "Low-frequency noise and phase noise behavior of advanced SiGe HBTs," 2001 IEEE MTT-S International Microwave Sympsoium Digest (Cat. No.01CH37157), Phoenix, AZ, USA, 2001, pp. 1705-1708 vol.3, doi: 10.1109/MWSYM.2001.967234.

[35] J. Raoult, F. Pascal, C. Delseny, M. Marin, and M. J. Deen, “Impact of carbon concentration on 1/f noise and random telegraph signal noise in SiGe:C heterojunction bipolar transistors,” *J Appl Phys*, vol. 103, no. 11, 2008, doi: https://doi.org/10.1063/1.2939252

[36] M. Seif et al., "Study of low frequency noise in advanced SiGe:C heterojunction bipolar transistors," 2014 44th European Solid State Device Research Conference (ESSDERC), Venice Lido, Italy, 2014, pp. 373-376, doi: 10.1109/ESSDERC.2014.6948838.

[37] M. Seif et al., "Characterization, modeling and comparison of 1/f noise in Si/SiGe:C HBTs issued from three advanced BiCMOS technologies," 2017 29th International Conference on Microelectronics (ICM), Beirut, Lebanon, 2017, pp. 1-4, doi: 10.1109/ICM.2017.8268847.

[38] B. Sagnes et al., "Low Frequency Noise in advanced 55nm BiCMOS SiGeC Heterojunction Bipolar Transistors: Impact of collector doping," 2017 International Conference on Noise and Fluctuations (ICNF), Vilnius, Lithuania, 2017, pp. 1-4, doi: 10.1109/ICNF.2017.7986001.

[39] J. D. Cressler, "Using SiGe HBT technology for extreme environment electronics," Proceedings of the Bipolar/BiCMOS Circuits and Technology Meeting, 2005., Santa Barbara, CA, USA, 2005, pp. 248-251, doi: 10.1109/BIPOL.2005.1555243.

[40] J. El Beyrouthy et al., "Effects of Total Ionizing Dose on 1-V and Low Frequency Noise characteristics in advanced Si/SiGe:C Heterojunction Bipolar Transistors," 2019 19th European Conference on Radiation and Its Effects on Components and Systems (RADECS), Montpellier, France, 2019, pp. 01-04, doi: 10.1109/RADECS47380.2019.9745680.

[41] J. El Beyrouthy et al., "Impact of Gamma irradiation on advanced Si/SiGe:C BiCMOS technology: comparison versus X-ray," 2020 20th European Conference on Radiation and Its Effects on Components and Systems (RADECS), Toulouse, France, 2020, pp. 1-4, doi: 10.1109/RADECS50773.2020.9857722.

[42] G. Prakash and N. Pushpa, "Application of Pelletron Accelerator to Study High Total Dose Radiation Effects on Semiconductor Devices," *Solid State Phenomena*, Aug. 2015, doi: https://doi.org/10.4028/www.scientific.net/ssp.239.37

[43] J. D. Cressler et al., "An investigation of the origins of the variable proton tolerance in multiple SiGe HBT BiCMOS technology generations," in IEEE Transactions on Nuclear Science, vol. 49, no. 6, pp. 3203-3207, Dec. 2002, doi: 10.1109/TNS.2002.805362.

[44] J. A. Babcock, J. D. Cressler, L. S. Vempati, S. D. Clark, R. C. Jaeger and D. L. Harame, "Ionizing radiation tolerance of high-performance SiGe HBT's grown by UHV/CVD," in IEEE Transactions on Nuclear Science, vol. 42, no. 6, pp. 1558-1566, Dec. 1995, doi: 10.1109/23.488750.

[45] A. K. Sutton et al., "A comparison of gamma and proton radiation effects in 200 GHz SiGe HBTs," in IEEE Transactions on Nuclear Science, vol. 52, no. 6, pp. 2358-2365, Dec. 2005, doi: 10.1109/TNS.2005.860728.

[46] J. Zhang *et al.*, "Impact of Bias Conditions on Total Ionizing Dose Effects of 60Coγ in SiGe HBT," in *IEEE Transactions on Nuclear Science*, vol. 63, no. 2, pp. 1251-1258, April 2016, doi: 10.1109/TNS.2016.2522158.

[47] D. Nergui et al., "Total-Ionizing-Dose Response of SiGe HBTs at Elevated Temperatures," in IEEE Transactions on Nuclear Science, vol. 69, no. 5, pp. 1079-1084, May 2022, doi: 10.1109/TNS.2022.3164327.

[48] P. Chevalier et al., "A 55 nm triple gate oxide 9 metal layers SiGe BiCMOS technology featuring 320 GHz fT / 370 GHz fMAX HBT and high-Q millimeter-wave passives," 2014 IEEE International Electron Devices Meeting, San Francisco, CA, USA, 2014, pp. 3.9.1-3.9.3, doi: 10.1109/IEDM.2014.7046978.

[49] S. A. Wartenberg, "Selected topics in RF coplanar probing," in IEEE Transactions on Microwave Theory and Techniques, vol. 51, no. 4, pp. 1413-1421, April 2003, doi: 10.1109/TMTT.2003.809184.

[50] V. Girones et al., "The Use of High-Energy X-Ray Generators for TID Testing of Electronic Devices," in IEEE Transactions on Nuclear Science, vol. 70, no. 8, pp. 1982-1989, Aug. 2023, doi: 10.1109/TNS.2023.3279626.

[51] S. Sharma, A. Sumathi, and C. Periasamy, "Photodetection Properties of ZnO/Si Heterojunction Diode: A Simulation Study," *IETE Technical Review*, vol. 34, no. 1, pp. 83–90, Feb. 2016, doi: https://doi.org/10.1080/02564602.2016.1145558

[52] J. El Beyrouthy, “Characterization and modeling of low frequencies noise in bipolar transistors developed in BiCMOS technology (55 nm node) for RF to THz applicationsés en technologie BiCMOS (nœud 55 nm) pour des applications RF et THz,” pp. 54-55,2020.

[53] M. Seif et al., "Low frequency noise measurements of advanced BiCMOS SiGeC Heterojunction Bipolar Transistors used for mm-Wave to terahertz applications," 2013 22nd International Conference on Noise and Fluctuations (ICNF), Montpellier, France, 2013, pp. 1-4, doi: 10.1109/ICNF.2013.6578977.

[54] Jin Tang, Guofu Niu, Joseph and Harame, "Impact of collector-base junction traps and high injection barrier effect on 1/f noise," 2003 Proceedings of the Bipolar/BiCMOS Circuits and Technology Meeting (IEEE Cat. No.03CH37440), Toulouse, France, 2003, pp. 175-178, doi: 10.1109/BIPOL.2003.1274961.

[55] C. Delseny, F. Pascal, S. Jarrix, and G. Lecoy, “Noise correlation measurements in bipolar transistors. II. Correlation between base and collector currents,” *Journal of Applied Physics*, vol. 81, no. 6, pp. 2658–2664, Mar. 1997, doi: https://doi.org/10.1063/1.363931.

[56] SS. P. O. Bruce, L. K. J. Vandamme and A. Rydberg, "Measurement of low-frequency base and collector current noise and coherence in SiGe heterojunction bipolar transistors using transimpedance amplifiers," in IEEE Transactions on Electron Devices, vol. 46, no. 5, pp. 993-1000, May 1999, doi: 10.1109/16.760408.

[57] C. Mukherjee et al., "Low-Frequency Noise in Advanced SiGe:C HBTs—Part II: Correlation and Modeling," in IEEE Transactions on Electron Devices, vol. 63, no. 9, pp. 3657-3662, Sept. 2016, doi: 10.1109/TED.2016.2588318.

[58] C. Mukherjee *et al.*, “Random telegraph noise in SiGe HBTs: Reliability analysis close to SOA limit,” *Microelectronics Reliability*, Jun. 2017,

doi: https://doi.org/10.1016/j.microrel.2017.05.001.

[59] V. N. Hegde et al., "A Comparison of Electron, Proton and Gamma Irradiation Effects on the I-V Characteristics of 200 GHz SiGe HBTs," in IEEE Transactions on Device and Materials Reliability, vol. 18, no. 4, pp. 592-598, Dec. 2018, doi: 10.1109/TDMR.2018.2875064.

[60] J. El Beyrouthy, “Characterization and modeling of low frequencies noise in bipolar transistors developed in BiCMOS technology (55 nm node) for RF to THz applicationsés en technologie BiCMOS (nœud 55 nm) pour des applications RF et THz,” pp.85-86,2020.

[61] O. Flament, S. Synold, J. de Pontcharra and S. Niel, "Radiation tolerance of NPN bipolar technology with 30 GHz Ft," 1999 Fifth European Conference on Radiation and Its Effects on Components and Systems. RADECS 99 (Cat. No.99TH8471), Fontevraud, France, 1999, pp. 401-405, doi: 10.1109/RADECS.1999.858615.

[62] J. M. Roldan, Guofu Niu, W. E. Ansley, J. D. Cressler, S. D. Clark and D. C. Ahlgren, "An investigation of the spatial location of proton-induced traps in SiGe HBTs," in IEEE Transactions on Nuclear Science, vol. 45, no. 6, pp. 2424-2429, Dec. 1998, doi: 10.1109/23.736481.

[63] J. El Beyrouthy, “Characterization and modeling of low frequencies noise in bipolar transistors developed in BiCMOS technology (55 nm node) for RF to THz applicationsés en technologie BiCMOS (nœud 55 nm) pour des applications RF et THz,” pp.86,2020.

[64] M. Seif *et al.*, “Dispersion study of DC and Low Frequency Noise in SiGe:C Heterojunction Bipolar Transistors used for mm-Wave to Terahertz applications,” *Microelectronics Reliability*, vol. 54, no. 9–10, pp. 2171–2175, Sep. 2014, https://doi.org/10.1016/j.microrel.2014.07.027

[65] J. El Beyrouthy, “Characterization and modeling of low frequencies noise in bipolar transistors developed in BiCMOS technology (55 nm node) for RF to THz applicationsés en technologie BiCMOS (nœud 55 nm) pour des applications RF et THz,” pp.106,2020.

[66] J. El Beyrouthy, “Characterization and modeling of low frequencies noise in bipolar transistors developed in BiCMOS technology (55 nm node) for RF to THz applicationsés en technologie BiCMOS (nœud 55 nm) pour des applications RF et THz,” pp.123,2020.